Biopolymer-templated deposition of ordered and polymorph TiO_2 thin films for improved SERS sensitivity

Qing Chen, Marie Betker, Constantin Harder, Calvin J. Brett, Matthias Schwartzkopf, Nils Ulrich, Maria E. Toimil-Molares, Christina Trautmann, L. Daniel Söderberg, Christian L. Weindl, Volker Körstgens, Peter Müller-Buschbaum, Mingming Ma, and Stephan V. Roth**

Dr. Q. Chen, M. Betker, C. Harder, Dr. C. J. Brett, Dr. M. Schwartzkopf, Prof. S. V. Roth
Deutsches Elektronen Synchrotron DESY, Notkestraße 85, 22607 Hamburg, Germany

Dr. Q. Chen, Prof. M. Ma
Hefei National Laboratory for Physical Sciences at Microscale, Department of Chemistry, University of Science and Technology of China, Jin-Zhai 96, 230026 Hefei, China, E-mail: mma@ustc.edu.cn

Prof. S. V. Roth, M. Betker, Prof. Dr. L. D. Söderberg
Fibre and Polymer Technology, KTH Royal Institute of Technology, Brinellvägen 8, 11428 Stockholm, Sweden, E-mail: svroth@kth.se

Dr. C. J. Brett
Department of Engineering Mechanics, Royal Institute of Technology KTH, Osquars Backe 18, 10044 Stockholm, Sweden

Dr. C. J. Brett, Prof. Dr. L. D. Söderberg
Wallenberg Wood Science Center, Royal Institute of Technology KTH, Teknikringen 52, 10044 Stockholm, Sweden

C. Harder, C. L. Weindl, Dr. V. Körstgens, Prof. P. Müller-Buschbaum
Lehrstuhl für Funktionelle Materialien, Physik Department, Technische Universität München, James-Franck Straße 1, 85748 Garching, Germany

Prof. P. Müller-Buschbaum
Heinz Maier-Leibnitz Zentrum (MLZ), Technische Universität München, Lichtenbergstraße 1, 85748 Garching, Germany

N. Ulrich, Dr. M. E. Toimil-Molares, Prof. C. Trautmann
Materials Research Department, GSI Helmholtz Center, Planckstraße 1, 64291 Darmstadt, Germany

Keywords: Bio-template, Semiconductor metal oxide nanomaterials, Atomic layer deposition, X-ray scattering, Surface enhanced Raman scattering

Titanium dioxide (TiO_2) is an excellent candidate material for semiconductor metal oxide-based substrates for surface enhanced Raman scattering (SERS). Bio-templated fabrication of TiO_2 thin-films with a three-dimensional network is a promising route for effectively transferring the morphology and ordering of the template into the TiO_2 layer. The control over the crystallinity of TiO_2 remains a challenge due to the low thermal stability of biopolymers. We report a novel

strategy of the cellulose nanofibril (CNF)-directed assembly of TiO_2/CNF thin films with tailored morphology and crystallinity as SERS substrates. Polymorphous TiO_2/CNF thin films with well-defined morphology are obtained by combining atomic layer deposition and thermal annealing. A high enhancement factor of 1.79×10^6 in terms of semiconductor metal oxide nanomaterial (SMON) - based SERS substrates is obtained from the annealed TiO_2/CNF thin films with a TiO_2 layer thickness of 10 nm fabricated on ITO, when probed by 4-mercaptobenzoic acid molecules. Common SERS probes down to 10 nM can be detected on these TiO_2/CNF substrates, indicating superior sensitivity of TiO_2/CNF thin films among SMON SERS substrates. This improvement in SERS sensitivity is realized through a cooperative modulation of the template morphology of the CNF network and the crystalline state of TiO_2.

1. Introduction

Surface-enhanced Raman scattering (SERS) substrates based on semiconductor metal oxide nanomaterials (SMONs) have attracted substantial attention for their potential applications in sensing of biomolecules,[1] trace detection of pollutants,[2] and monitoring the catalytic reactions[3] due to their low-cost, high stability and biocompatibility.[4] Besides, SMONs show a greater variety of crystalline states,[5] as well as a wider range of optical and electrical properties in comparison to noble metals,[6] which can be tailored to meet the specific demands in SERS applications. Titanium dioxide (TiO_2) nanoparticles (NPs) are among the most appropriate materials for fabricating high-performance SERS substrates in the area of SMONs.[7] However, the bottleneck problem of TiO_2 NPs-based SERS substrates is the low sensitivity compared to noble metal nanomaterials.[8] The theoretical maximum enhancement factor (EF) for SMON SERS substrates based on the charge-transfer (CT) mechanism has been estimated to be 10^6,[1] while the experimental EF values for practical TiO_2 SERS substrates are mostly only in the range of 10^3 to 10^4.[9]

Two strategies have been carried out to improve the EF values of TiO_2-based SERS substrates. The first option is to tailor the crystalline state of TiO_2 for improving the interactions between TiO_2-based substrate and the analytes. The most investigated crystalline parameters include the crystallinity, crystallite size, as well as the polymorph ratio for example the rutile to anatase crystalline phase ratio of TiO_2.[10] Nonetheless, both the control over the crystallinity and crystallite size could be a "double-edged sword" for improving the SERS performance of TiO_2 substrates. The high degree of crystallinity as well as a high concentration of surface defects are two desired but contradictory properties for a superior SERS performance of SMONs.[11] When the annealing temperature raises, the crystallinity of TiO_2 increases but the concentration of surface defects decreases. Besides, at an increased annealing temperature the anatase-to-rutile phase transformation of TiO_2 has to be taken into account. Although the rutile phase displays a much lower SERS activity compared to the anatase phase, the synergistic effect between the rutile and anatase TiO_2 leads to a higher SERS activity than pure anatase TiO_2 due to the additional charge transfer from rutile to anatase TiO_2 despite the intrinsic charge transfer from anatase TiO_2 to the analytes. Whereas polymorphous TiO_2 with a low rutile-to-anatase ratio could not bring about the synergistic effect, an overly high rutile-to-anatase ratio will lead to a decreased SERS activity as well. Moreover, the SERS intensity of TiO_2 increases within a certain range of particle size, reaching a maximum and declines at larger sizes subsequently.[12] Therefore, the preparation of TiO_2 thin films with desired crystallinity state is a crucial requirement for fabrication. Thermal annealing is one of the most commonly used methods for controlling the crystalline state of TiO_2.[13] However, the morphology and optical properties of the TiO_2 thin films could be significantly affected by thermal annealing.[14]

Thus, the preservation of the tailored morphology is another important requirement for the fabrication of TiO_2 despite its crystalline state. This leads to the second option, which is to regulate the surface morphology of the TiO_2 layer to enhance the interactions between the laser and the substrate. The specific surface area of the TiO_2 layer influences the density of available

active sites for SERS activity,[15] and the interconnected network within the TiO_2 layer influences the rate of charge-carrier transfer. The most investigated morphological parameters include the shape, size and ordering of TiO_2.[16] The control over the morphology of TiO_2 nanomaterials can be achieved by precise surface engineering methodologies. An effective method for controlling the dimensions, periodicity, and structure at both nano- and microscale is to employ templates with desired 3D architectures.[17] Commonly used templating material varies from hard/inorganic materials to soft/organic materials. Representative inorganic templates for TiO_2 fabrication include carbon materials, as well as metal oxide particles such as ZnO and Al_2O_3.[18] In contrast to hard templates, soft templates such as synthetic and natural polymers are particularly attractive due to the relative ease of chemical modification. A few bio-templates including the proteins in tobacco mosaic virus, ferritin[19] and butterfly wings[20] have been successfully exploited to prepare porous TiO_2 thin films. On the other hand, being engineered from the most abundant biopolymers,[21] nanocellulose (NC) represents another type of bio-templates,[22] which typically includes cellulose nanocrystals (CNCs), cellulose nanofibrils (CNFs) and bacterial cellulose (BC).[23] Although CNCs[24] and BC[25] have demonstrated promising possibilities for fabricating 3D templates of TiO_2 thin films, the progress over CNF-templated TiO_2 thin films is still very limited.

Nonetheless, CNFs hold great potential for templating the morphology of TiO_2 thin films in three aspects. (1) CNFs feature high flexibility and mechanical strength,[26] which creates an interconnected network to support the complex morphologies of TiO_2.[27] (2) CNFs could be fabricated into hierarchically ordered materials, which provides a wide range of templating substrate architectures[28] including two-dimensional (2D) arrays,[29] and three-dimensional (3D) scaffolds.[30] (3) CNFs could be used as a standard deposition matrix for nanoparticles with a homogeneous distribution at a low agglomeration rate,[31] which confers the resulting composite films with distinct optical properties. However, the use of CNF templates presents a challenge for traditional coating processes such as sol-gel,[32] layer-by-layer (LBL)

deposition,[33] chemical vapor deposition,[34] sputtering,[35] lithography,[36] and their combinations,[37] as they are limited in their ability preserving the topography of the template. On the contrary, atomic layer deposition (ALD) is a powerful coating technique based on self-limiting surface reactions, which enables deposition of highly conformal thin-films onto 3D templates with high precision.[38] ALD coating enables a well-defined thickness and the fulfillment of deposited material into the nanometer sized pores within the template. With the improvement in ALD technology, which made the deposition at low temperature possible, TiO_2 could be deposited without destruction of the bio-template.[39] However, the CNF-templated assembly of TiO_2 as SERS substrates has not been reported yet.

In the present study, we report a versatile strategy for the fabrication of TiO_2/CNF thin films that feature an improved SERS sensitivity with a precisely controlled morphology and crystalline state. The 3D network of CNFs with well-defined morphology was templated to fabricate a conformal TiO_2 layer *via* ALD coating, which is thermally annealed to achieve the desired crystalline state (**Figure 1**). The influence of three key factors on the SERS performance of TiO_2/CNF thin films are studied: (1) The morphology of the CNF template, which regulates the ordering of TiO_2 layer, and is achieved *via* oblique incidence spraying (OIS)[40] of CNFs onto Si and ITO substrates. ITO substrates are commonly used as electrodes, and the nanostructures on ITO provide a patterned template for the OIS of cellulose in comparison to the smooth Si substrates. (2) Thermal annealing of TiO_2/CNF thin films to control the crystalline state of TiO_2. Since the crystalline size and rutile-to-anatase ratio of TiO_2 increase simultaneously with the annealing temperature, an annealing temperature of 450 °C was applied to achieve a relatively higher crystallite size of anatase TiO_2 and a relatively lower rutile-to-anatase ratio.[41] (3) Different deposition thickness of the TiO_2 layer, which is expected to influence the specific surface area of the layer due to the limitation in the precision of the ALD coating, and therefore the crystallinity of TiO_2. In this respect, a thickness of 10 nm is representing a 2D TiO_2 thin layer with high specific area and a thickness of 60 nm is

representing a bulky 3D layer with a lower specific area considering the radii of TiO_2 NPs, which is around 6.5 nm deduced from grazing incidence small angle X-ray scattering (GISAXS). The as-prepared TiO_2/CNF thin films are probed by atomic force microcopy (AFM) and scanning electron microscopy (SEM) for the local examination of the surface, and the cross-section morphology as well as estimation of the specific surface area. As a complementary method, GISAXS and grazing-incidence wide-angle X-ray scattering (GIWAXS) techniques are used to investigate the in-plane 3D ordering and crystalline state of the thin films.[42] Finally, the performance of TiO_2/CNF thin films as SERS substrates is investigated, and the impact of the template morphology, crystallinity state, and specific surface area of the TiO_2/CNF thin films on the enhancement factors of the analytes is characterized by Raman spectroscopy. Collectively, this strategy offers a high tunability in the tailoring of the SERS performance of SMONs by modulating the template morphology and the crystalline properties of SMONs.

2. Results and discussion

2.1. Morphology

We adopted the following name conventions for samples as indicated in **Table S1**: (1) The Si and ITO substrates are noted as "Si" and "ITO". (2) The CNF thin films OIS-coated on Si and ITO are referred as "Si/CNF" and "ITO/CNF", which are noted as "Si/CNFa" and "ITO/CNFa" after annealing at 450 °C, respectively. (3) The ALD-coated samples with a TiO_2 layer thickness (δ_T) of 10 nm and 60 nm are noted as "Si or ITO/CNF/$TiO_2$10" and "Si or ITO/CNF/$TiO_2$60", which are referred as "Si or ITO/CNF/$TiO_2$10a" and "Si or ITO/CNF/$TiO_2$60a" after annealing, respectively. For example, the "ITO/CNF/$TiO_2$60a" sample refers to the annealed sample with TiO_2 (δ_T = 60 nm) ALD-coated on CNF thin film fabricated on ITO. **Figure 2** shows the surface morphology of the TiO_2/CNF thin films fabricated on Si (a) and ITO (b). Multiple line-cuts, combined with the fitting of the power spectral density (PSD) distribution of the AFM images,

are conducted to extract the morphological parameters at different length scales, since the large nanostructures in the range of $k < 0.006$ nm^{-1} is beyond the resolution of the PSD distribution. Before annealing, a uniform distribution of cellulose bundles is observed in both the Si/CNF and ITO/CNF samples. Although the Si/CNF sample displays no preferential orientation of cellulose bundles, the ITO/CNF sample shows an ordering of knot-like morphology, which is composed of densely-packed cellulose bundles with a diameter ($Ø$) of $Ø_{CNF1}$ = (190 ± 9) nm, and an edge-to-edge distance (d) of d_{CNF1} = (65 ± 10) nm connected by loosely-aligned cellulose bundles (**Figure S2**). The CNF thin films were fully covered by TiO_2 NPs with $Ø_{TiNP1}$ = (15 ± 3) nm in the Si/CNF/$TiO_2$10, Si/CNF/$TiO_2$60, ITO/CNF/$TiO_2$10 and ITO/CNF/$TiO_2$60 samples despite the variations in δ_T as well as the template morphology (**Figure S1**). The agreement in size and distribution of TiO_2 NPs originates from the conformality of the ALD coating technique and is mainly determined by the coating conditions. Taking the Si-based samples as an example, the higher magnification images (**Figure S3**) clearly show a necklace architecture of the TiO_2 layer with the length scale (L) ranging from 152 nm < L_{CNF1} < 179 nm. This suggests the structural replication of TiO_2 necklace of the cellulose bundles, which originates from the conformal binding of TiO_2 NPs to the cellulose bundles.

After annealing at 450 °C, TiO_2/CNF thin films undergo different degrees of morphological changes depending on the template morphology and the layer thickness of TiO_2. Two major differences between Si- and ITO-based samples are observed. The first difference lies in the shape and size of TiO_2 nanostructures. In the Si-based samples (Si/CNF/$TiO_2$10a and Si/CNF/$TiO_2$60a), two TiO_2 nanostructures with $Ø_{TiNP1}$ = (100 ± 5) nm (**Figure S4**) and $Ø_{TiNP2}$ = (19 ± 4) nm (**Figure S1**) are detected, which may correspond to the mixture of aggregated and individual TiO_2 NPs or polymorphous TiO_2 with different crystalline domain sizes. While the small TiO_2 nanostructures bind to cellulose bundles to form a necklace architecture, the large and uniformly distributed TiO_2 nanostructures are more densely distributed in the Si/CNF/$TiO_2$10a (d_{TiNP1} = 174 ± 18 nm) than in the Si/CNF/$TiO_2$60a sample (d_{TiNP1} = 201 ± 9

nm), as shown in **Figure S4**. On the other hand, the ITO-based ITO/CNF/$TiO_2$10a and ITO/CNF/$TiO_2$60a samples display a terrace-like morphology (**Figure S5**), with discs ($Ø_{TiNP1}$ = 193 ± 22 nm) which are composed of closely-packed TiO_2 NPs with a diameter of $Ø_{TiNP2}$ = 34 ± 5 nm (**Figure S1**). The distinct morphology of the TiO_2 layer in Si-based (Si/CNF/$TiO_2$10a, Si/CNF/$TiO_2$60a) and ITO-based (ITO/CNF/$TiO_2$10a, ITO/CNF/$TiO_2$60a) samples is related to the crystallization degree of TiO_2 NPs, which will be discussed in detail in the "Crystallinity" section.

In agreement with the line-cut results, fitting analysis of the PSD data reveals similar sizes and distributions of TiO_2 NPs among the Si/CNF/$TiO_2$10, Si/CNF/$TiO_2$60, ITO/CNF/$TiO_2$10 and ITO/CNF/$TiO_2$60 samples (**Figure S6, Figure S7**). The nanostructure with radii (R) of R_{TiNP2} = (59 ± 9) nm and center-to-center distance (D) of D_{TiNP2} = (295 ± 55) nm are observed, with "$R = Ø / 2$" and "$D = 2 \times R + d$" corresponding to the parameters in the line-cut analysis (**Table S2**). After thermal annealing, the PSD distributions of TiO_2/CNF thin films display similar patterns as their corresponding templates. Especially, the extracted parameters in the ITO/CNF/$TiO_2$10a sample (R_{TiNP1} = 77 ± 11 nm and D_{TiNP1} = 247 ± 55 nm) are almost consistent with the ITO/CNF sample (R_{CNF1} = 79 ± 9 nm D_{CNF1} = 245 ± 39 nm), indicating the replication of the knot-like morphology of the CNF template. The values from PSD fitting are smaller than that from the line-cut analysis due to averaging of the nanostructures of different sizes.

The second difference between Si- and ITO-based samples lies in the distribution of the TiO_2 nanostructures, which directly reflects the template morphology and the template replication degree. Two levels of structural replication exist in our systems: (1) the CNF layer is expected to template the morphology of TiO_2 layer by ALD coating, and (2) the substrate morphology is expected to transfer to the CNF template by OIS coating. At the first level, the necklace architecture signifies the morphology of TiO_2 templated by the CNF layer. According to **Figure 2 (a)**, the necklace architecture is more obvious in Si- than ITO-based samples, and is better

seen in samples with δ_T = 10 nm than that with δ_T = 60 nm (**Figure S3**). In Si-based samples, the necklace architecture of the TiO_2 layer become more prominent after annealing, with a larger length scale of 177 nm < L_{CNF1} < 226 nm (**Figure S4**), which suggests the better interaction between TiO_2 nanostructures and cellulose bundles, and a higher degree of structural replication facilitated by the partial carbonization of CNFs.

At the second level, the Si-based samples replicate the substrate morphology and form a relatively smoother surface due to the lack of morphological features of the Si substrate. In the ITO-based samples, the morphology of the TiO_2 layer does not reveal the fibrous architecture of CNFs, but reflects the knot-like morphology of the ITO and the CNF thin film coated on ITO, which can be observed from the strong morphological similarities among the ITO/CNF/$TiO_2$10a, ITO/CNF/$TiO_2$60a, ITO/CNF and ITO samples **(Figure 2b**). This indicates a weaker interaction between TiO_2 nanostructures and individual cellulose bundles due to the large diameter of TiO_2 nanostructures in the ITO/CNF/$TiO_2$10a and ITO/CNF/$TiO_2$60a samples. However, due to the larger diameter of the TiO_2 nanostructure ($Ø_{TiNP2}$ =193 ± 22 nm) than the CNF knots ($Ø_{CNF1}$ = 190 ± 9 nm), and the smaller edge-to-edge distance of TiO_2 nanostructure (d_{TiNP1} = 35 ± 10 nm) than the knots (d_{TiNP1} = 65 ± 10 nm), TiO_2 terrace is more likely to grow on the CNF knots, leading to the replication of the CNF template (**Figure S5**). Furthermore, the cross-sectional SEM images clearly show the knot-like morphology (**Figure 2c**) and the terrace morphology of the TiO_2 layer in the ITO/CNF/$TiO_2$10a samples (**Figure 2d**). The similarity in the distribution patterns of the ITO/CNF/$TiO_2$10 and ITO/CNF/$TiO_2$10a samples indicates the successful structural templating at the TiO_2 / CNF and the CNF / ITO interfaces **(Figure S8)**. Collectively, both the Si- and ITO-based samples successfully replicated the layer morphology of CNFs, but the layer replication is more obvious in ITO-based samples due to the knot-like morphology. In Si-based samples, the small TiO_2 nanostructure dominates, and the smaller diameter of this nanostructure compared to the distance between cellulose bundles made it possible to replicate the individual cellulose bundles. On the other hand, in ITO-based samples,

the sizeable TiO_2 nanostructure dominates, and the larger diameter of this nanostructure compared to the distance between cellulose bundles blocked the replication of the individual cellulose bundles.

Apart from the morphological evolution parallel to the film surface, the surface roughness of the TiO_2/CNF thin films also varies with δ_T and the template morphology (**Figure 2e**). Obtained from the WsXM software v5.0,[43] we found that the root-mean-square (RMS) roughness of the ITO/CNF sample (σ_{rms} =5.2 ± 0.3 nm) is almost two times of the ITO (σ_{rms} =2.6 ± 0.2 nm). The increase in roughness of the OIS-coated CNF template compared to the substrate indicates that the surface morphology is transferred and enhanced from ITO to the CNF layer. Furthermore, the ITO-based TiO_2/CNF thin films display a higher roughness than their Si-based counterparts (e. g. Si/CNF/$TiO_2$10 and ITO/CNF/$TiO_2$10, Si/CNF/$TiO_2$10a and ITO/CNF/$TiO_2$10a), which is also related to a lower roughness of the CNF template in the Si/CNF sample (σ_{rms} =3.7 ± 0.2 nm). This can be rationalized by the fact that cellulose bundles are more likely to distribute onto the convex surface of ITO particles due to the mutual effect of shear strength and spatial effect, while they distribute uniformly on Si substrate under the same fabrication process. Before annealing, the roughness of the Si- or ITO-based samples are slightly smaller than their corresponding CNF template (Si/CNF and ITO/CNF). Also the roughness in samples with δ_T = 10 nm are marginally higher than that with δ_T = 60 nm, which decreased from σ_{rms} = (3.5 ± 0.3) nm (Si/CNF/$TiO_2$10) to σ_{rms} = (3.4 ± 0.2) nm (Si/CNF/$TiO_2$60) on Si, and from σ_{rms} = (4.6 ± 0.4) nm (ITO/CNF/$TiO_2$10) to σ_{rms} = (4.3 ± 0.3) nm (ITO/CNF/$TiO_2$60) on ITO with the increase of δ_T, respectively. This is due to the limitation in size of TiO_2 NPs determined by the ALD conditions, leading to a decreased ability for TiO_2 NPs to fulfill the underlying layer, and thus a decreased template replication efficiency with an increased ALD thickness.

After thermal annealing, the roughness in all TiO_2/CNF thin films increased, which are σ_{rms} = (5.0 ± 0.2 nm) in the Si/CNF/$TiO_2$10a, σ_{rms} = (8.4 ± 0.5 nm) and σ_{rms} = (8.4 ± 0.5 nm) in the ITO/CNF/$TiO_2$10a and ITO/CNF/$TiO_2$60a samples, respectively. This might originate from the

partial collapse of the voids within the CNF network formed during OIS coating, which leads to a higher roughness contrast between the collapsed and remaining part among the CNF network. The increase is more significant in ITO- than Si-based samples, which might be related to the larger TiO_2 nanostructures' size in ITO-based samples.

2.2. Crystallinity

GIWAXS is performed to investigate the effect of thermal annealing on the crystalline state of ALD-coated TiO_2 NPs and the CNF template (**Figure S9**). **Figure 3a** and **Figure S10** illustrate the GIWAXS patterns of TiO_2/CNF thin films fabricated on Si and ITO, respectively. The GIWAXS patterns of the CNF templates and their corresponding substrates are shown in **Figure S11**. To investigate the influence of ALD-coated TiO_2 on the crystallinity of cellulose, the GIWAXS patterns of pristine CNF thin film without TiO_2 coating are also investigated (**Figure S12**). In the GIWAXS patterns of Si-based samples, the broad peak in the range of 1.5 $Å^{-1} < q < 2.5$ $Å^{-1}$ is observed in the Si/CNF/$TiO_2$10 and Si/CNF/$TiO_2$60 samples, which is attributed to the $(1\bar{1}0)$ scattering plane of CNFs and the amorphous state of ALD-coated TiO_2 NPs. However, two sharp peaks become prominent after thermal annealing, which indicate the evolution of $(1\bar{1}0)$ and (200) scattering planes of CNFs. Two broad and pronounced peaks in the range of 2.5 $Å^{-1} < q < 2.8$ $Å^{-1}$ are identified as the (101) and (110) scattering planes of anatase and rutile phase of TiO_2 crystallites, respectively. Besides, despite the weakening of the anatase and rutile scattering planes of TiO_2 due to the strong scattering of ITO in the ITO/CNF/$TiO_2$10a and ITO/CNF/$TiO_2$60a samples, the peak in the range of 1.7 $Å^{-1} < q < 2.2$ $Å^{-1}$ clearly indicates the crystallization of CNFs. The agreement between Si- and ITO-based samples demonstrate that the important role of annealing conditions in the phase transition of TiO_2 and crystallization of CNF.

To further analyze the evolution of the crystallinity of TiO_2 and CNFs, the 2D GIWAXS profiles are radially integrated using the GIXSGUI software v1.7.1 (**Figure S1**).[44] Before thermal annealing, the Si/CNF/$TiO_2$10 and Si/CNF/$TiO_2$60 samples show a broad peak over

the range of 0.5 $Å^{-1} < q < 2.5$ $Å^{-1}$ in the 1D GIWAXS patterns (**Figure 3b**), which is attributed to the amorphous state of TiO_2 and the Si substrate. Additionally, the marked small peak at q_{TA} = 2.5 $Å^{-1}$ (101) indicates the existence of a small amount of anatase TiO_2. After annealing, the rutile TiO_2 peak appears at q_{TR} = 2.8 $Å^{-1}$ (110), and the anatase peak at q_{TA} = 2.5 $Å^{-1}$ becomes more pronounced. This suggests an increase in the crystallite size, and a partial thermally-induced anatase-to-rutile phase transition of TiO_2. The circumstance for ITO-based samples is quite similar, indicating polymorphous TiO_2 after annealing (**Figure 3c**). Moreover, the crystallinity of CNFs undergoes tremendous changes after thermal annealing. In TiO_2/CNF thin films, the CNF crystalline domains show three broad peaks at q_{CNFa} = 1.6 $Å^{-1}$ ($1\bar{1}0$), q_{CNFb} = 2.1 $Å^{-1}$ (200), and q_{CNFc} = 3.4 $Å^{-1}$ (004), which belong to type I cellulose structure. After annealing, two prominent characteristic peaks at q_{CNFb} = 2.1 $Å^{-1}$ and q_{CNFd} = 2.0 $Å^{-1}$ (110) are detected, demonstrating the formation of type II cellulose.[45] The decrease in the peak intensity of (004) and ($1\bar{1}0$) is due to the transformation of cellulose from type I to II and a partial carbonization of CNFs, suggesting that the remaining CNFs became more thermodynamically stable **(Figure S13)**. On the other hand, the annealed CNF thin films without ALD-coated TiO_2 display no characteristic peaks of cellulose, indicating the total carbonization of CNFs (**Figure S14**). Collectively, the ALD-coated TiO_2 offers a protecting layer for CNFs, which leads to a limited carbonization degree, meaning an increased thermal stability providing a strong support for the crystallized TiO_2 nanostructures.

To investigate the formation of TiO_2 polymorph, the Bragg peaks in the range 0.5 $Å^{-1} < q < 3.0$ $Å^{-1}$ are deconvoluted (**Figure S15**). The crystalline domain size (*DnP*) of TiO_2 is estimated from the full width at half maximum (FWHM) of the fitted (101) and (110) scattering peaks deducing the instrumental resolution measured from LaB_6, *via* the adapted Debye-Scherrer formula for grazing-incidence scattering.[46] Before annealing, the *DnP* of amorphous/anatase TiO_2 NPs varies in the range of (*DnP* = 14.2 ± 0.4) nm among the Si/CNF/$TiO_2$10, Si/CNF/$TiO_2$60, ITO/CNF/$TiO_2$10 and ITO/CNF/$TiO_2$60 samples (**Figure 3d**). After annealing,

a slight increase in *DnP* of anatase TiO_2 is observed, reaching *DnP* = (17.5 ± 0.3) nm. This is consistent with the Ostwald ripening effect, in which the atomic diffusion leads to the growth and coalescence of the TiO_2 crystalline phase.[47] The *DnP* values of rutile TiO_2 range from (*DnP* = 34 ± 3) nm in spite of the differences in δ_T and template morphology. The *DnP* of rutile TiO_2 is smaller in Si- than in the ITO-based samples, corroborating the AFM results. Besides, the rutile-to-anatase ratio ($\chi_{R/A}$) of TiO_2 polymorph [48] are $\chi_{R/A}$ = 0.21, $\chi_{R/A}$ = 0.45, $\chi_{R/A}$ = 0.26, and $\chi_{R/A}$ = 0.59 among the Si/CNF/$TiO_2$10a, Si/CNF/$TiO_2$60a, ITO/CNF/$TiO_2$10a and ITO/CNF/$TiO_2$60a samples (**Figure 3e**), which are within the suitable range (17.6 % < $\chi_{R/A}$ < 33.3%) of rutile-to-anatase ratio for optimal SERS activity of TiO_2 [49]. The relatively higher $\chi_{R/A}$ of the ITO-based samples coincides with the higher σ_{rms} from AFM analysis, contributing to a higher specific surface area to act as the active sites for nucleation of the rutile TiO_2 crystallites (**Table S3**). The values of surface area are obtained by the Gwyddion software v2.55 from AFM images under the scan size of 3 × 3 μm^2.[50] By assuming that the mass of TiO_2 increases proportionally with δ_T, we are able to compare the relative specific area among the samples.

2.3. Topography

Complementary to the AFM and SEM measurements, which study the local morphology of the film surface or cross-section, GISAXS is performed to probe into the topography of the entire film (**Figure S9**). 2D GISAXS data of the TiO_2/CNF thin films and their corresponding templates are shown in **Figure 4a,b** and **Figure S16**, respectively. To obtain a quantitative analysis of the nanostructures of TiO_2 NPs and the CNF template, horizontal line-cuts were taken along q_y direction at q_z = 0.65 nm^{-1} in Si- and q_z = 0.75 nm^{-1} in ITO-based samples (**Figure S17**). The horizontal line-cuts are subsequently analyzed by a model described in our previous studies to obtain statistically averaged values of the morphological features of TiO_2 and CNFs in real-space.[51] The model is based on cylindrical objects describing the cellulose-based

nanostructures and spherical objects describing the TiO_2-based nanostructures and ITO (**Table S4**). The lower layer is fitted prior to the upper layer to reduce the complexity of the fits and reduce the number of free parameters in the fits. For example, the ITO/CNF/$TiO_2$10 sample is fitted by the successive addition of the fit functions of ITO, CNFs and TiO_2. Based on this model, the best fits are shown as the green dashed lines in **Figure 4c,f**, and the center-to-center distances "*D*" (**Figure 4d,e**) as well as the radii "*R*" (**Figure 4 f,g**) are extracted.

In agreement with our previous results (**Figure S18**),[52] three cylindrical structures are identified for the CNF template on Si, with R_{CNF1} = (27 ± 3) nm, R_{CNF2} = (11.0 ± 1.9) nm, R_{CNF3} = (2.1 ± 0.3) nm and D_{CNF1} = (73 ± 2) nm, D_{CNF2} = (75 ± 3) nm, and D_{CNF3} = (11.0 ± 0.9) nm in the Si/CNF sample, which correspond to the empty voids within the CNF network (3D), individual cellulose bundle (2D), and cellulose fibrils (1D), respectively. Similarly, three cylindrical structures are observed for the CNF template on ITO besides the prominent nanostructure of ITO with R_{ITO} = (50 ± 5) nm and D_{ITO} = (150 ± 9) nm in the ITO/CNF sample. Apart from the nearly identical 1D and 2D nanostructures of CNFs compared to the Si/CNF sample, the cylindrical and knot-like nanostructure (R_{CNF1} = 90 ± 13 nm, D_{CNF1} = 255 ± 20 nm) is identified, which agrees with our AFM analysis. Before annealing, TiO_2 shows a nanostructure with 5.1 nm < R_{TiNP2} < 7.9 nm and 12.9 nm < D_{TiNP2} < 17.6 nm. The "*R*" and "*D*" values of this nanostructure correspond to individual TiO_2 NPs that build up the conformal TiO_2 layer. In the range of 0.01 nm^{-1} < *q* < 0.06 nm^{-1}, a superstructure with 49.5 nm < R_{TiNP1} < 87.0 nm is observed, which corresponds to orderly-assembled TiO_2 agglomerates, and the size TiO_2 agglomerates (R_{TiNP1}) varies significantly among samples with δ_T = 60 nm and δ_T = 10 nm. In the Si/CNF/$TiO_2$10 sample, the TiO_2 agglomerates with R_{TiNP1} = (55 ± 6) nm in a distance of D_{TiNP1} = (340 ± 10) nm and individual TiO_2 NPs with R_{TiNP2} = (6.5 ± 1.1) nm in a distance of D_{TiNP2} = (16 ± 2) nm are identified. In the Si/CNF/$TiO_2$60 sample, the agglomerates show R_{TiNP1} = (66 ± 6) nm in a distance of D_{TiNP1} = (340 ± 15) nm, and individual TiO_2 NPs show R_{TiNP2} = (6.8 ± 0.9) nm in a distance of D_{TiNP2} = (15.5 ± 1.5) nm (**Figure 4d,e**). The TiO_2 agglomerates

in the Si/CNF/$TiO_2$60 sample display larger radii (R_{TiNP1} = 66 ± 6 nm) compared to the Si/CNF/$TiO_2$10 sample (R_{TiNP1} = 55 ± 6 nm), indicating that the ALD-coated TiO_2 NPs gradually assemble into orderly-arranged nanostructures horizontally as the layer thickness increases on Si. The ITO-based ITO/CNF/$TiO_2$10 and ITO/CNF/$TiO_2$60 samples show similar parameters compared to the Si/CNF/$TiO_2$10 and Si/CNF/$TiO_2$60 samples (**Table S5, Table S6**), with the radii of TiO_2 agglomerates being R_{TiNP1} = (60 ± 7) nm and R_{TiNP1} = (75 ± 12) nm, as well as the radii of TiO_2 NPs being R_{TiNP2} = (6.2 ± 1.1) nm and R_{TiNP2} = (7.0 ± 0.5) nm, respectively. Besides, the same center-to-center distance of D_{TiNP1} = (350 ± 32) nm and D_{TiNP2} = (15.0 ± 2.1) between the ITO/CNF/$TiO_2$10 and ITO/CNF/$TiO_2$60 samples are detected (**Figure 4g,h**).

As observed from the AFM and GIWAXS analysis, the TiO_2/CNF thin films undergo substantial structural changes, including the partial carbonization of the CNFs, and the crystallization of TiO_2 NPs after annealing. For CNFs, the individual cellulose fibrils (R_{CNF1}, D_{CNF1}) in both Si- and ITO-based samples are preserved. The cellulose bundles with R_{CNF2} = (7.8 ± 2.5) nm and D_{CNF2} = (75 ± 3) nm[31, 52] which are hardly visible in the GISAXS data of the ALD-coated samples (Si/CNF/$TiO_2$10, Si/CNF/$TiO_2$60, ITO/CNF/$TiO_2$10 and ITO/CNF/$TiO_2$60), are clearly identified in the Si/CNF/$TiO_2$10a, ITO/CNF/$TiO_2$10a and ITO/CNF/$TiO_2$60a (**Figure 3c,f, Figure S19**). Besides, despite the identical D_{CNF2} of cellulose between the annealed samples (Si/CNF/$TiO_2$10a, Si/CNF/$TiO_2$60a, ITO/CNF/$TiO_2$10a and ITO/CNF/$TiO_2$60a) and their corresponding CNF templates (Si/CNF and ITO/CNF), the radii of these nanostructures drop to R_{CNF2} = (7.8 ± 2.5) nm compared to the CNF template (R_{CNF2} = 11.0 ± 1.9 nm). This reflects the increase of the electron density contrast due to the tubular structure of the partially carbonized cellulose bundles or the decrease in the radii of cellulose bundles (**Figure S20**). At a higher order, 3D CNF nanostructures' preservation varies between Si- and ITO-based samples. The empty voids of the 3D CNF network in Si-based samples (Si/CNF/$TiO_2$10a and Si/CNF/$TiO_2$60a) disappear after annealing (seen as R_{CNF1} = 27 ± 3 nm,

D_{CNF1} = 73 ± 2 nm in **Figure 4e**), which might be the result of the collapse of the 3D CNF architecture during the intensive crystallization of TiO_2. This agrees with the increased RMS roughness after thermal annealing in the Si-based samples from the AFM analysis. However, in ITO-based samples, the 3D nanostructure of CNF knots is preserved, with R_{CNF1} = (85 ± 10) nm and D_{CNF1} = (123 ± 5) nm.

For TiO_2-related nanostructures, the radii of individual TiO_2 NPs on Si-based samples (Si/CNF/$TiO_2$10a, Si/CNF/$TiO_2$60a) slightly increase to R_{TiNP3} = (8.1 ± 1.3) nm and R_{TiNP3} = (8.3 ± 2.0) nm with the center-to-center distance being constant of D_{TiNP3} = (18.5 ± 3.3) nm and D_{TiNP3} = (18.0 ± 2.5) nm, signifying the formation of anatase TiO_2 NPs with larger crystallite sizes after annealing. The fitted "*R*" and "*D*" values of rutile TiO_2 crystallites is nearly consistent between the Si/CNF/$TiO_2$10a and Si/CNF/$TiO_2$60a samples, which are R_{TiNP2} = (16.5 ± 2.9) nm with D_{TiNP2} = (39 ± 5) nm, and R_{TiNP2} = (16.9 ± 2.0) nm and D_{TiNP2}= (36 ± 5) nm. This can be rationalized with the *DnP* analysis from GIWAXS measurement, which suggests the diameter of rutile TiO_2 crystallites in the range of 30.7 nm < *DnP* < 36.8 nm. Besides, the agglomerates of rutile TiO_2 are identified, with R_{TiNP1} = (95 ± 5) nm, D_{TiNP1} = (180 ± 8) in the Si/CNF/$TiO_2$10a, and R_{TiNP1} = (105 ± 4) nm, D_{TiNP1} = (200 ± 10) in the Si/CNF/$TiO_2$60a samples, which corroborates the line-cut results from the AFM analysis. Similar to the Si-based samples, two rutile TiO_2 nanostructures and one anatase TiO_2 nanostructure are observed in ITO-based samples, with the "terrace" of rutile TiO_2 composed of densely-clustered rutile TiO_2 crystallites. In the ITO/CNF/$TiO_2$10a sample, the anatase TiO_2 NPs show R_{TiNP3} = (8.3 ± 2.1) nm and D_{TiNP3} = (19.6 ± 4.2) nm, while the rutile TiO_2 NPs display a radius of R_{TiNP2} = (17.0 ± 2.5) nm with a distance of D_{TiNP2} = (39 ± 3) nm, and R_{TiNP1} = (113 ± 5) nm with a distance of D_{TiNP1} = (275 ± 25) nm (**Figure 4g,h**). Similarly, the ITO/CNF/$TiO_2$60a sample contains anatase TiO_2 NPs with R_{TiNP3} = (8.4 ± 1.7) nm and D_{TiNP3} = (19.0 ± 3.2) nm, as well as two rutile TiO_2 nanostructures with R_{TiNP2} = (17.6 ± 2.0) nm and D_{TiNP2} = (37 ± 3) nm, as well as R_{TiNP1} = (125 ± 15) nm and

D_{TiNP1} = (255 ± 25) nm. The sizes and distributions of rutile TiO_2 crystallites confirm the *DnP* results from GIWAXS measurements.

2.4. Model of evolution in morphology and crystallinity

At the same annealing conditions, the morphological and crystalline parameters of TiO_2 are dominated by the ALD coating conditions and the template morphology of the CNFs (**Figure 5**). The structural evolution of TiO_2 NPs is affected by the structural replication of the CNFs at three different scales. Firstly, as indicated by the AFM and SEM analysis, the TiO_2 layer replicates of the morphology of the CNF layer in both the Si- and ITO-based samples due to the conformity of ALD coating.

Secondly, the replication of individual cellulose bundles depends on the interaction between TiO_2 and CNF nanostructures, which could be influenced by the morphology of CNF and the crystallization of TiO_2. The morphology of the CNF template is significantly dominated by the 3D architectures of CNF, which includes the empty voids of the CNF network in Si-based samples, and the knots in ITO-based samples. The empty voids in the CNF template on Si disappeared after annealing, while the knots on ITO are preserved. A higher ratio of the removed 3D architectures in the CNF template is estimated on Si than ITO substrate. This is due to the weaker support of Si compared to the knots structure supported by ITO particles.

For the evolution of TiO_2 crystallites, the replication of the individual cellulose bundles depends on the size of TiO_2 NPs, with the small anatase TiO_2 NPs in Si-based samples displaying a better replication of these bundles compared to the large rutile TiO_2 NPs in ITO-based samples, in which the size of rutile TiO_2 is almost two times of anatase TiO_2. The rutile TiO_2 (R_{TiNP2}, D_{TiNP2}) on ITO grows into large and coalescent nanostructures, which limit their horizontal growth. This results in a terrace morphology due to its higher specific area to create more nucleation sites at the anatase / rutile interface in ITO-based samples. In Si-based samples, the lower rutile-to-anatase ratio of TiO_2 crystalline phases, and the smaller diameter of anatase TiO_2

compared to the distance between cellulose bundles lead to a better replication of these bundles. However, in ITO-based samples, the higher specific surface area of the ITO/CNF sample leads to a larger rutile-to-anatase ratio, and the larger diameter of rutile TiO_2 crystallites compared to the distance between cellulose bundles weakens the interaction between TiO_2 and CNFs. This results in a poor replication of the individual cellulose bundles. While AFM techniques focus locally on the surface morphology, GISAXS accesses provides statistical information of the complete film. The variation in the size and distance of the nanostructures extracted from the PSD analysis of AFM images and GISAXS fit results are interpreted as a gradient distribution of the TiO_2 nanoparticles along the thickness direction of the film, which shows larger radii on the film surface than the ones underneath (**Table S7**).

Thirdly, the replication of the topography of cellulose bundles is preserved in spite of the TiO_2 crystallization and the template morphology. The GISAXS and GIWAXS results reveal the partially-carbonized cellulose bundles with a smaller radius underlying the TiO_2 layer compared to the pristine bundles, which is undetectable from AFM analysis. The results from the above measurements are in good well agreement and are sufficient to study the size and distribution of the TiO_2 and CNF nanostructures. Therefore, TiO_2 polymorphs with desired crystallite size and rutile-to-anatase ratio are obtained by controlling the template morphology of the CNF layer and the deposition thickness of TiO_2. Besides, although the morphology of cellulose bundles is replicated at different degrees due to the crystallization of TiO_2, the topography of cellulose bundles at the TiO_2 / CNF interface is preserved during annealing. The layer replication of TiO_2 layer on both, Si and ITO substrates demonstrates the ability of CNFs as a robust and precise structure-directing template.

2.5. SERS performance

Different from the noble metal nanomaterials, the SERS performance of SMONs depends significantly on the combination of morphological and crystalline properties including the

shape, size, ordering and crystallinity of the SMON nanostructures.[16] Therefore, the influence of these parameters on the SERS performance of the TiO_2/CNF thin films are investigated by using 4-mercaptobenzoic acid (4-MBA) and crystal violet (CV) as the standard probes. The SERS spectra with continuously varying concentrations of 4-MBA (from 1×10^{-4} to 1×10^{-8} M) on the TiO_2/CNF thin films are provided in **Figure 6a** and **Figure S21**. The marked peak positions are consistent with the characteristic SERS signals of 4-MBA molecules.[10, 53] The strong bands at 1594 cm^{-1} and 1078 cm^{-1} are assigned to aromatic ring vibrations, and the weak bands at 1148 cm^{-1} and 1182 cm^{-1} are attributed to the C-H deformation modes (**Table S9**). The SERS spectra of 4-MBA adsorbed on TiO_2/CNF thin films are enhanced[12] and is different from the typical Raman spectra of 4-MBA ethanol solution in both the intensity and position of the peaks.[54] Furthermore, the selective enhancement of the 1148 cm^{-1} peak suggests the charge transfer from TiO_2 to 4-MBA molecules.[55] Additionally, the narrow 1078 cm^{-1} peak of 4-MBA overlaps with the broad peak characteristic of CNF (1097 cm^{-1}). Thus, the Raman spectra of CNFs is deducted in the following EF analysis.

It can be observed from **Figure 6b** that 4-MBA molecules exhibit a higher enhancement at the 1594 cm^{-1} and 1078 cm^{-1} bands when adsorbed on the annealed ITO/CNF/$TiO_2$10a and ITO/CNF/$TiO_2$60a samples than on their pristine ITO/CNF/$TiO_2$10 and ITO/CNF/$TiO_2$60 samples. The highest SERS enhancement is received on the ITO/CNF/$TiO_2$10a sample at the Raman shift of 1078 cm^{-1}, in which the concentration of 4-MBA as low as (1×10^{-8} M) can still be clearly distinguished (**Figure 6a**). Besides, **Figure S22 (a)** suggests a linear relationship between the peak intensity and the concentration of 4-MBA, demonstrating its potential application for quick analysis. To quantitatively analyze the SERS performance of TiO_2/CNF thin films, the enhancement factors at the 1078 and 1594 cm^{-1} bands of 4-MBA at the concentration of 10^{-5} M were calculated. According to the standard equation,[56] the ITO/CNF/$TiO_2$10a sample shows an EF value of 1.79×10^6 at 1078 cm^{-1} (**Figure 6e**), which indicates an outstanding sensitivity among plasmon-free TiO_2-based SERS substrates (**Table**

S9). The high EF achieved by TiO_2/CNF is even comparable to some noble metal-based SERS substrates that typically show much higher EF than TiO_2-based SERS substrates.[57] In contrast, the EF value of the Si/CNF/$TiO_2$10 sample is estimated to be 5.25×10^5 under the same conditions. Additionally, after storing in a sealed sample box at ambient condition for 45 days, the SERS spectra of the ITO/CNF/$TiO_2$10a sample at 10^{-5} M 4-MBA shows a substantial similarity to that of the freshly fabricated samples (**Figure 6f**). These results demonstrate excellent stability of TiO_2/CNF thin films as a practical SERS substrate, which could originate from the support of CNF matrix to the polymorphous TiO_2 NPs.

Similar results of TiO_2/CNF thin films are obtained by using CV as the analyte (**Figure 6c, Figure S23**). In **Figure 6d**, the SERS intensities of the C-C stretching band at 915 cm^{-1}, in-plane C-H stretching band at 1180 cm^{-1}, and C-C stretching band at 1623 cm^{-1} in the ITO/CNF/$TiO_2$10a sample is much stronger than the corresponding ITO/CNF/$TiO_2$60a, Si/CNF/$TiO_2$10a and ITO/CNF/$TiO_2$10 reference samples (**Table S7**). The linear relationship between the peak intensity at 915 cm^{-1} and the concentrations of CV for the ITO/CNF/$TiO_2$10a sample is observed (**Figure S22 (b)**). The lowest detection limit of the ITO/CNF/$TiO_2$10a sample is at 10^{-7} M level, which is slightly lower than the sensitivity with 4-MBA as the analyte. This could be related to a stronger interaction between TiO_2 and 4-MBA than that between TiO_2 to CV molecules. The superior SERS performance of the ITO/CNF/$TiO_2$10a sample can also be observed by comparing the EF values calculated from the three characteristic bands of CV. The EF values measured at 10^{-5} M CV in ITO-based samples follow the identical trend as the circumstance of 4-MBA: ITO/CNF/$TiO_2$10a > ITO/CNF/$TiO_2$60a > ITO/CNF/$TiO_2$10 > ITO/CNF/$TiO_2$60 (**Figure 6d**). For comparison, the EF values of plasmon-free TiO_2 SERS substrates previously reported are shown in **Table S9**.

The SERS enhancement of TiO_2/CNF thin films is proposed to stem from the charge transfer of the TiO_2 NPs assisted by multiple light scattering at the film surface. To further understand the variation of the CT efficiency between the ALD-coated and thermally annealed samples,

we measured the sheet resistance of the TiO_2/CNF thin films. The sheet resistance of the ALD-coated Si/CNF/$TiO_2$10, Si/CNF/$TiO_2$60, ITO/CNF/$TiO_2$10 and ITO/CNF/$TiO_2$60 samples are *Rs* = (21.6 ± 0.04) Ω/sqr, *Rs* = (16.6 ± 0.05) Ω/sqr, *Rs* = (19.5 ± 0.04) Ω/sqr, and *Rs* = (15.1 ± 0.05) Ω/sqr. After thermal annealing, the sheet resistance decreased to *Rs* = (7.1 ± 0.06) Ω/sqr, *Rs* = (6.9 ± 0.05) Ω/sqr, *Rs* = (6.7 ± 0.04) Ω/sqr, and *Rs* = (6.6 ± 0.04) Ω/sqr in the Si/CNF/$TiO_2$10a, Si/CNF/$TiO_2$60a, ITO/CNF/$TiO_2$10a and ITO/CNF/$TiO_2$60a samples, respectively (**Figure S24**). The decrease in sheet resistance is attributed to a more favorable crystallinity state which enables higher electron mobility,[56] and the generation of free electrons to improve the carrier concentrations for SERS enhancement. The relatively lower sheet resistance of the ITO/CNF/$TiO_2$10a and ITO/CNF/$TiO_2$60a compared to the Si/CNF/$TiO_2$10a and Si/CNF/$TiO_2$60a samples could be related to the higher crystallinity (larger crystallite size) and the higher rutile-to-anatase ratio of TiO_2.

To summarize, the SERS activity of the TiO_2/CNF thin films depends on the layer morphology, topography and the crystalline state of TiO_2. The superior SERS performance of the ITO/CNF/$TiO_2$10a sample originates from the CT resonance based on the combination of appropriate crystallite size of anatase TiO_2 and an appropriate rutile-to-anatase ratio, which is further amplified by a relatively high degree of ordering at the film surface. The crystalline property of TiO_2 is the most crucial factor in the SERS performance of TiO_2/CNF thin films. The small crystallite size of anatase TiO_2 in the ALD-coated ITO/CNF/$TiO_2$10 sample is less favorable for SERS enhancement of the adsorbed molecules than the thermally-annealed ITO/CNF/$TiO_2$10a sample. Besides, one reason for the higher SERS performance of the ITO/CNF/$TiO_2$10a than the Si/CNF/$TiO_2$10a sample is related to its higher rutile-to-anatase ratio (**Figure 3e**). The synergistic effect between rutile and anatase phases of TiO_2 provides an additional CT from rutile to anatase TiO_2 besides the intrinsic CT from anatase TiO_2 to the probe molecules, which is responsible for the higher SERS enhancement in the polymorphous than mono-phased TiO_2-based substrates. However, an overly rutile-to-anatase ratio is

unfavorable for improving the CT resonance in polymorph TiO_2 due to the lower SERS activity of rutile compared to anatase phase. Therefore, the ITO/CNF/$TiO_2$60a sample is less sensitive in the analytes' SERS enhancement than the ITO/CNF/$TiO_2$10a sample.

Besides, template morphology is another essential factor in the SERS performance of TiO_2/CNF thin films in amplifying the surface resonance of the Raman signals,[58] and in providing access to high specific surface area. On the one hand, the regularity of the TiO_2 nanostructures with the support of CNF knots leads to a higher SERS activity in ITO- than Si-based samples by multiple light scattering. This is another reason for the higher SERS enhancement of the ITO/CNF/$TiO_2$10a than the Si/CNF/$TiO_2$10a sample. On the other hand, the ITO-based samples generally show a larger specific area than the Si-based samples. The difference in specific surface area is enlarged by the crystallization of TiO_2, in which the samples with larger specific surface area creating more anatase-to-rutile nucleation sites, and thus a higher crystallite size of TiO_2 is obtained (**Figure 3d**). Nonetheless, the effect of template morphology appeared to be less critical than the crystalline state of TiO_2. Besides, the ITO/CNF/$TiO_2$10 sample shows a higher SERS activity than the ITO/CNF/$TiO_2$60 sample, demonstrating the vital role of the specific surface area regardless of the crystalline state and template morphology.

3. Conclusion

This study demonstrates a new strategy to fabricate bio-templated, well-ordered, and polymorphous TiO_2/CNF thin films with significantly enhanced SERS sensitivity through the combined action of (1) oblique incidence spraying to prepare a highly-ordered CNF template, (2) atomic layer deposition to transfer the template morphology into the TiO_2 layer, and (3) thermal annealing to obtain a desired crystalline state. The template morphology shows a significant influence on the order and morphology of the resulting TiO_2 layer. Thermal annealing exhibits a profound effect on the topography and crystalline state of TiO_2 and CNFs.

An improved templating effect of CNFs is observed after annealing, with a higher RMS roughness due to the collapse of the empty voids in the 3D CNF network. And the partially carbonized cellulose bundles of the remaining CNF network contribute to the higher electron density of the polymorphous TiO_2 NPs. Collectively, the TiO_2/CNF thin film with a TiO_2 layer thickness of 10 nm on ITO substrate shows an excellent SERS performance with an EF value of 1.79×10^6, which is higher than the average EF for TiO_2-based, plasmon-free SERS substrates *via* CT mechanism. This is achieved by the appropriate rutile-to-anatase ratio and crystallite size of anatase TiO_2, accompanied by the high ordering degree of the TiO_2 layer. These results demonstrate the important roles of the layer morphology, topography and crystallinity of TiO_2 in the SERS performance in the CNF-templated TiO_2 thin films. A high SERS sensitivity is achieved at the orderly-assembled and polymorphous TiO_2 layer, which opens the possibility of fabricating SMONs with tailored SERS sensitivity at an industrial scale. For future studies, we believe that the method for the CNF-directed assembly of TiO_2 nanoparticles could apply to fabricate a wider range of semiconductor metal oxide films, and the templating role of CNFs could be extended from the bottom to the top layer in a multiple-layered thin film via layer-by-layer deposition.

4. Experimental Section/Methods

Chemicals and materials: 0.07 wt % aqueous solution of 2,2,6,6-tetramethylpiperidine-1-oxyl radical (TEMPO)-CNF with a surface charge of 800 μmol/g and a radius of around 2.5 nm was dispersed by sonification and centrifugation to prepare CNF thin films. Si wafers (Silicon Materials, USA) and ITO glass slides (SOLEMS, France) with the same surface area of (25 × 25 mm^2) were used as substrates. Si wafers were sonicated with acetone for 15 min and then sequentially cleaned with isopropanol and deionized water, followed by an acid bath (87.5 mL hydrogen peroxide 30%, 190 mL 96 % sulfuric acid, and 37.5 mL deionized water) at 80 °C for 15 min. ITO glass slides were cleaned with deionized water and then sequentially treated with

alcohol, acetone, and isopropanol for 10 min. All solvents were purchased from Carl Roth GmbH, Germany. Deionized water was used throughout the experiment. CV and 4-MBA of analytical grade were purchased from Sigma-Aldrich, Germany. All the chemicals were used without further purification.

Oblique incidence spraying: Layer-by-layer spray-coating was performed by a spray-coating device (Compact JAU D555000, Spray Systems, Germany). In our previous work, we have developed a standard deposition procedure for spray-coating of uniform CNF thin films with a thickness of 200 nm. Herein, in order to fabricate a CNF thin film with well-defined orientation, the standard spray-coating procedure is slightly modified. The substrate was placed at an oblique angle of 10° with respect to the spray coating direction. The distance between the nozzle and the substrate was kept at 100 mm. The preparation is conducted at room temperature (T = 23 °C, RH = 50%). For each spray pulse, the deposition condition was 0.1 s spraying and the waiting time was elongated to 45 s for complete evaporation of the solvent. To minimize the film inhomogeneity resulting from the spray-cone, the substrate is rotated at 90° after each spray pulse. Therefore, after four spray pulses, the substrate is rotated back to the starting direction, which we noted as a spray cycle. The spray cycles were repeated 40 times to prepare a CNF thin film with a thickness of 200 nm.

Atomic layer deposition (ALD) and thermal annealing: The ALD of TiO_2 layer was conducted by our collaborators from GSI Helmholtzzentrum für Schwerionenforschung, Darmstadt, Germany with a Picosun R200 Basic ALD device. The ALD of the TiO_2 layer was performed at 110°C, and the tetraisopropoxide precursor was preheated to 70 °C in the reservoir. The procedures were set as follows: (a) a 5.2 s dose of titanium tetraisopropoxide (TTIP) with 60 standard cubic centimeter per minute (sccm) N_2 carrier gas flow; (b) a 50 s purge of oversupplied TTIP with 120 sccm N_2; (c) a 0.4 s dose of H_2O with 200 sccm N_2 as carrier gas flow; (d) a 50 s purge of oversupplied H_2O and by-products. The four-step sequence constitutes one ALD cycle and the number of ALD cycles were adjusted for obtaining TiO_2 layer with a

desired thickness. For the TiO_2 layer with δ_T = 10 nm, the number of cycles was 909, and the error in layer thickness is ± 0.19 nm; and for the TiO_2 layer with δ_T = 60 nm, the number of cycles was 5454, and the error in layer thickness is ± 1.09 nm. The as-prepared TiO_2/CNF thin films were thermally annealed in a furnace (FP1100, Borel Swiss) at 450 °C for 30 min. The annealing conditions were chosen based on literature to produce a mixed-phase TiO_2 layer with the desired rutile-to-anatase ratio.[41]

Morphology characterization (AFM, SEM): The AFM images were acquired with an NTEGRA probe Nano-Laboratory (NT-MDT, Russia) in the semi-contact mode. ETALON cantilevers with a tip radius of 10 nm and a resonant frequency of 90 kHz (NT-MDT, Russia) were used for all samples. For each sample, 5 pictures of 2D topography maps were taken with a scan size of 3 × 3 μm^2 and 1 × 1 μm^2. AFM data analysis, including line-cuts, and average roughness was done by WSxM v5.0 software. For the cross-sectional analysis, the samples were frozen in liquid nitrogen to avoid delamination of the film upon fracture. SEM images were taken with a Zeiss Gemini NVision 40 field emission microscope operated at 5 kV and a working distance of around 5.6 mm.

Grazing-incidence X-ray scattering: Since the as-prepared TiO_2/CNF samples are thin films, we employed grazing-incidence X-ray scattering techniques to study the structural information at the TiO_2 / CNF interface. The in-depth morphology and crystallinity of the samples were investigated with GISAXS and GIWAXS, respectively. The X-ray scattering experiments were performed at the MiNaXS/P03 beamline of the PETRA III storage ring at DESY, Hamburg.[59] The energy of the X-ray was 11.8 keV (λ = 1.05 Å) with a beam size of 80 × 56 μm^2 (horizontal × vertical). One beam stop was used to shield the specular reflected beam. A sketch of the GISAXS and GIWAXS setup is shown in **Figure S9**, with α_i and α_f representing the incident and exit angles, respectively. The sample-to-detector distance (*SDD*) was kept at SDD_{GISAXS} = (3930 ± 2) mm in GISAXS and SDD_{GIWAXS} (312 ± 2) mm in GIWAXS measurements. 2D GISAXS data were collected by PILATUS 300k detector (Dectris Ltd., Switzerland) with a

pixel size of 172 × 172 μm^2 and GIWAXS data were collected by LAMBDA 750k detector (X Spectrum GmbH, Germany) with a pixel size of 55 × 55 μm^2. The incident angle α_i was set at 0.4° for GISAXS, and 0.11° for GIWAXS measurements. A lateral scanning with a step size of 100 μm by moving the sample through the beam in the lateral direction was performed to avoid X-ray beam induced alteration of the samples. Each GISAXS pattern was acquired for 1 s, and each GIWAXS pattern was acquired for 0.1 s. 1D intensity distributions were extracted from the 2D GISAXS data using the Directly Programmable Data Analysis Kit software (DPDAK) v1.4.1 [60] and fitted by minimum chi-square estimation with cumulative cylindrical and spherical form factors including 1D structure factors as previously reported by Schaffer *et al*.[51] For GIWAXS, the q_r, q_z plots were transformed by Grazing-incidence X-ray Scattering Graphical User Interface software (GIXSGUI) v1.7.135. Peak positions and intensity of the peak in the q_r, q_z plots were extracted to provide information about crystalline dimensions, degree of crystallinity and the rutile-to-anatase ratio in the TiO_2/CNF thin films. The rutile-to-anatase ratio ($\chi_{R/A}$) is calculated based on a formula reported by Khatun et al.,[48]

$$\chi_{R/A} = 1 / (1 + 1.26 \times I_R / I_A), \quad (1)$$

where I_R and I_A are the intensities of the (110) and (101) diffraction peaks of rutile and anatase TiO_2 in the 1D GIWAXS data, respectively.

Crystallite domain size (*DnP*) of TiO_2 was calculated with an adapted form of the Debye-Scherrer formula,[46]

$$DnP = 2\pi K / \Delta q_B, \quad (2)$$

where Δq_B is the FWHM of the (101) or the (110) peaks, and K the particle shape factor, which is taken as 0.94 valid for spherical crystallites with cubic symmetry.

Conductivity measurement: The measurements were performed using a four-point setup T2001A (Ossila Ltd., UK) and the raw data were analyzed using Ossila Sheet Resistance (v2.0.3.3, Ossila Ltd, UK) software. The probes were spring-loaded and separated by 1.27 mm, the set target current was 10 mA and the voltage increment was 0.1 V. Sheet resistance

measurements were performed 25 times and 2048 samples per point were measured. The sample size for conductivity measurements was 20 × 80 mm^2.

SERS and Raman spectroscopy: The samples were cut into 4 × 4 mm^2 for SERS measurement. Aqueous solution of CV, and ethanol solution of 4-MBA were diluted to desired concentrations as analytes for SERS (10^{-5} to 10^{-8} M) and Raman (10^{-3} to 10^{-5}) analysis. To make the surface of the substrates covered with a monolayer of CV and 4-MBA sufficiently, 3 μL of the analyte solutions were directly dropped on the surface of the TiO_2/CNF thin films and their corresponding templates and substrates. For Raman analysis, 3 μL of the solution of analyte was dropped onto the Si and ITO substrates, respectively. After the evaporation of water or ethanol, Raman signals were collected on the surface of these samples. SERS spectra were collected on a Raman spectrometer (SENTERRA, Bruker GmbH) with an excitation wavelength of 532 nm at a laser power of 4 mW and an objective of 50× magnification. The accumulation time was 20 s and the time for data acquiring was 4 s. Raman spectra were collected and averaged from five different points. Raman data was analyzed by OPUS v6 software. The enhancement factor (EF) of the thin films can be calculated according to the following equation.[56]

$$EF = (I_{SERS} / N_{SERS}) / (I_0 / N_0) \quad (3)$$

$$N_{SERS} = Sc_{SERS} VN_A / S' \quad (4)$$

$$N_0 = c_0 ShN_A \quad (5)$$

where I_0, c_0, and N_0 are the intensities of the characteristic vibration bands, the concentration and the corresponding number of molecules in Raman spectra. I_{SERS}, c_{SERS} and N_{SERS} are the intensities of the characteristic vibration bands, the concentration and the corresponding number of molecules in SERS spectra. h, S, S', V, and N_A are the focused depth, the area of the laser spot, the area of the TiO_2-containing substrate, the volume of analyte, and Avogadro constant.

Supporting Information

Supporting Information is available from the Wiley Online Library.

Acknowledgements

Q.C., S.V.R. and M.M. acknowledge the financial support from the Helmholtz-OCPC program (No.20191004). Q.C. and S.V.R thank Prof. Ilya Sergeev, the responsible scientist at P01 of PETRA III P01, for giving us access to the Raman spectroscopy. S.V.R. acknowledge the kind financial support from the DESY strategic fund (DSF) "Investigation of processes for spraying and spray-coating of hybrid cellulose-based nanostructures". M.B. acknowledge the financial support from the DSF "Investigation of processes for fabricating functional multi-component stacks based on nanopaper and spray-coating". V.K. and P.M.B. acknowledge funding from TUM.solar in the context of the Bavarian Collaborative Research Project Solar Technologies Go Hybrid (SolTech), the Deutsche Forschungsgemeinschaft (DFG) under Germany´s Excellence Strategy-EXC 2089/1-390776260 (e-conversion) and the International Research Training Group 2022 Alberta/Technical University of Munich International Graduate School for Environmentally Responsible Functional Hybrid Materials (ATUMS). All GISAXS and GIWAXS measurements were carried out at the light source PETRA III at DESY, a member of the Helmholtz Association (HGF).

Received: ((will be filled in by the editorial staff))
Revised: ((will be filled in by the editorial staff))
Published online: ((will be filled in by the editorial staff))

References

[1] I. Alessandri, J. R. Lombardi, *Chem. Rev.* **2016**, 116, 14921.

[2] W. Ji, Y. Wang, I. Tanabe, X. Han, B. Zhao, Y. Ozaki, *Chem. Sci.* **2015**, 6, 342.

[3] W. Song, W. Ji, S. Vantasin, I. Tanabe, B. Zhao, Y. Ozaki, *J. Mater. Chem. A* **2015**, 3, 13556.

[4] H. K. Lee, Y. H. Lee, C. S. L. Koh, Q. G. C. Phan, X. Han, C. L. Lay, H. Y. F. Sim, Y. Kao, Q. An, X. Y. Ling, *Chem. Sco. Rev.* **2019**, 48, 731.

[5] X. Wang, L. Guo, *Angew. Chem. Int. Ed.* **2020**, 59, 4231.

[6] a) J. Yan, W. Feng, J.-Y. Kim, J. Lu, P. Kumar, Z. Mu, X. Wu, X. Mao, N. A. Kotov, *Chem. Mater.* **2019**, 32, 476; b) S. Y. Yu, G. Schrodj, K. Mougin, J. Dentzer, J. P. Malval, H. W. Zan, O. Soppera, A. Spangenberg, *Adv. Mater.* **2018**, 30, 1805093.

[7] a) X. Zheng, F. Ren, S. Zhang, X. Zhang, H. Wu, X. Zhang, Z. Xing, W. Qin, Y. Liu, C. Jiang, *ACS Appl. Mater. Interfaces* **2017**, 9, 14534; b) A. Musumeci, D. Gosztola, T.

Schiller, N. M. Dimitrijevic, V. Mujica, D. Martin, T. Rajh, *J. Am. Chem. Soc.* **2009**, 131, 6040.

[8] a) S. Laing, L. E. Jamieson, K. Faulds, D. Graham, *Nat. Rev. Chem.* **2017**, 1, 0060; b) X. Yan, Q. Chen, Q. Song, Z. Huo, N. Zhang, M. Ma, *Nano Res.* **2020**, 14, 275.

[9] a) B. Qiu, M. Xing, Q. Yi, J. Zhang, *Angew. Chem. Int. Ed.* **2015**, 54, 10643; b) D. Qi, L. Lu, L. Wang, J. Zhang, *J. Am. Chem. Soc.* **2014**, 136, 9886.

[10] X. Wang, W. Shi, S. Wang, H. Zhao, J. Lin, Z. Yang, M. Chen, L. Guo, *J. Am. Chem. Soc.* **2019**, 141, 5856.

[11] G. Song, W. Gong, S. Cong, Z. Zhao, *Angew. Chem. Int. Ed.* **2021**, 60, 5505.

[12] X. Xue, W. Ji, Z. Mao, H. Mao, Y. Wang, X. Wang, W. Ruan, B. Zhao, J. R. Lombardi, *J. Phys. Chem. C* **2012**, 116, 8792.

[13] J. B. Joo, I. Lee, M. Dahl, G. D. Moon, F. Zaera, Y. Yin, *Adv. Funct. Mater.* **2013**, 23, 4246.

[14] A. Dualeh, N. Tétreault, T. Moehl, P. Gao, M. K. Nazeeruddin, M. Grätzel, *Adv. Funct. Mater.* **2014**, 24, 3250.

[15] Y. Bai, H. Yu, Z. Li, R. Amal, G. Q. M. Lu, L. Wang, *Adv. Mater.* **2012**, 24, 5850.

[16] a) I. Alessandri, *J. Am. Chem. Soc.* **2013**, 135, 5541; b) J. Lin, W. Ren, A. Li, C. Yao, T. Chen, X. Ma, X. Wang, A. Wu, *ACS Appl. Mater. Interfaces* **2020**, 12, 4204.

[17] M. E. Lamm, K. Li, J. Qian, L. Wang, N. Lavoine, R. Newman, D. J. Gardner, T. Li, L. Hu, A. J. Ragauskas, H. Tekinalp, V. Kunc, S. Ozcan, *Adv. Mater.* **2021**, 33, 2005538.

[18] a) H. Li, Q. Zhou, Y. Gao, X. Gui, L. Yang, M. Du, E. Shi, J. Shi, A. Cao, Y. Fang, *Nano Res.* **2015**, 8, 900; b) J. T. Park, W. S. Chi, D. K. Roh, S. H. Ahn, J. H. Kim, *Adv. Funct. Mater.* **2013**, 23, 26.

[19] A. K. M. Knez, C. Wege, U. Gosele, H. Jeske, K. Nielsch, *Nano Lett.* **2006**, 6, 1172.

[20] R. E. Rodriguez, S. P. Agarwal, S. An, E. Kazyak, D. Das, W. Shang, R. Skye, T. Deng, N. P. Dasgupta, *ACS Appl. Mater. Interfaces* **2018**, 10, 4614.

[21] A. Ivanova, D. Fattakhova-Rohlfing, B. E. Kayaalp, J. Rathousky, T. Bein, *J. Am. Chem. Soc.* **2014**, 136, 5930.

[22] Y. Pei, L. Wang, K. Tang, D. L. Kaplan, *Adv. Funct. Mater.* **2021**, 31.

[23] M. Kaushik, A. Moores, *Green Chem.* **2016**, 18, 622.

[24] a) M. K. Khan, M. Giese, M. Yu, J. A. Kelly, W. Y. Hamad, M. J. MacLachlan, *Angew. Chem. Int. Ed.* **2013**, 52, 8921; b) K. E. Shopsowitz, A. Stahl, W. Y. Hamad, M. J. MacLachlan, *Angew. Chem. Int. Edit.* **2012**, 51, 6886.

[25] a) H. Xie, C. Yang, K. K. Fu, Y. Yao, F. Jiang, E. Hitz, B. Liu, S. Wang, L. Hu, *Adv. Energy Mater.* **2018**, 8, 1703474; b) X. Ma, Y. Lou, X.-B. Chen, Z. Shi, Y. Xu, *Chem. Eng. J.* **2019**, 356, 227.

[26] N. Mittal, F. Ansari, V. K. Gowda, C. Brouzet, P. Chen, P. T. Larsson, S. V. Roth, F. Lundell, L. Wagberg, N. A. Kotov, L. D. Soderberg, *ACS Nano* **2018**, 12, 6378.

[27] A. J. Svagan, M. A. S. A. Samir, L. A. Berglund, *Adv. Mater.* **2008**, 20, 1263.

[28] B. Thomas, M. C. Raj, A. K. B, R. M. H, J. Joy, A. Moores, G. L. Drisko, C. Sanchez, *Chem. Rev.* **2018**, 118, 11575.

[29] E. Kontturi, P. Laaksonen, M. B. Linder, Nonappa, A. H. Groschel, O. J. Rojas, O. Ikkala, *Adv. Mater.* **2018**, 30, 1703779.

[30] R. T. Olsson, M. A. Azizi Samir, G. Salazar-Alvarez, L. Belova, V. Strom, L. A. Berglund, O. Ikkala, J. Nogues, U. W. Gedde, *Nat. Nanotechnol.* **2010**, 5, 584.

[31] Q. Chen, C. J. Brett, A. Chumakov, M. Gensch, M. Schwartzkopf, V. Körstgens, L. D. Söderberg, A. Plech, P. Zhang, P. Müller-Buschbaum, S. V. Roth, *ACS Appl. Nano Mater.* **2021**, 4, 503.

[32] N. Li, L. Song, L. Bießmann, S. Xia, W. Ohm, C. J. Brett, E. Hadjixenophontos, G. Schmitz, S. V. Roth, P. Müller-Buschbaum, *Adv. Mater. Interfaces* **2019**, 6, 1900558.

[33] M. A. Khan, S. Z. Islam, S. Nagpure, Y. He, N. Wanninayake, R. L. Palmer, J. Strzalka, D. Y. Kim, B. L. Knutson, S. E. Rankin, *J. Phys. Chem. C* **2019**, 124, 1958.

[34] J. Shi, C. Sun, M. B. Starr, X. Wang, *Nano Lett.* **2011**, 11, 624.

[35] J. E. Yoo, K. Lee, M. Altomare, E. Selli, P. Schmuki, *Angew. Chem. Int. Ed.* **2013**, 52, 7514.

[36] M. Luo, X. Hu, *J. Vac. Sci. Technol. B* **2020**, 38, 062604.

[37] J. Y. Yu, S. Landis, P. Fontaine, J. Daillant, P. Guenoun, *Soft Matter* **2020**, 16, 8179.

[38] S. M. George, *Chem. Rev.* **2010**, 110, 111.

[39] J.-P. Niemelä, G. Marin, M. Karppinen, *Semicond. Sci. Technol* **2017**, 32, 093005.

[40] R. Blell, X. Lin, T. Lindstrom, M. Ankerfors, M. Pauly, O. Felix, G. Decher, *ACS Nano* **2017**, 11, 84.

[41] a) I. S. Cho, Z. Chen, A. J. Forman, D. R. Kim, P. M. Rao, T. F. Jaramillo, X. Zheng, *Nano Lett.* **2011**, 11, 4978; b) R. Tao, J. Wu, H. Xue, X. Song, X. Pan, X. Fang, X. Fang, S. Dai, *J. Power Sources* **2010**, 195, 2989.

[42] a) J. Wakita, S. Jin, T. J. Shin, M. Ree, S. Ando, *Macromolecules* **2010**, 43, 1930; b) A. Mahmood, J.-L. Wang, *Solar RRL* **2020**, 4, 2000337.

[43] I. Horcas, R. Fernandez, J. M. Gomez-Rodriguez, J. Colchero, J. Gomez-Herrero, A. M. Baro, *Rev. Sci. Instrum.* **2007**, 78, 013705.

[44] Z. Jiang, *J. Appl. Crystallogr.* **2015**, 48, 917.

[45] P. Tingaut, T. Zimmermann, G. Sèbe, *J. Mater. Chem.* **2012**, 22, 20105.

[46] a) A. R. Bushroa, R. G. Rahbari, H. H. Masjuki, M. R. Muhamad, *Vacuum* **2012**, 86, 1107; b) D. M. Smilgies, *J. Appl. Crystallogr.* **2009**, 42, 1030.

[47] M. H. W. Lee, *J. Phys. Chem. C* **2010**, 114, 6917.

[48] N. Khatun, Anita, P. Rajput, D. Bhattacharya, S. N. Jha, S. Biring, S. Sen, *Ceram. Int.* **2017**, 43, 14128.

[49] L. Yang, M. Gong, X. Jiang, D. Yin, X. Qin, B. Zhao, W. Ruan, *J. Raman Spectrosc.* **2015**, 46, 287.

[50] D. Nečas, P. Klapetek, *Cent. Eur. J. Phys.* **2012**, 10, 181.

[51] a) C. J. Schaffer, C. M. Palumbiny, M. A. Niedermeier, C. Jendrzejewski, G. Santoro, S. V. Roth, P. Müller-Buschbaum, *Adv. Mater.* **2013**, 25, 6760; b) W. Wang, L. Song, D. Magerl, D. Moseguí González, V. Körstgens, M. Philipp, J.-F. Moulin, P. Müller-Buschbaum, *Adv. Funct. Mater.* **2018**, 28.

[52] a) C. J. Brett, N. Mittal, W. Ohm, M. Gensch, L. P. Kreuzer, V. Körstgens, M. Månsson, H. Frielinghaus, P. Müller-Buschbaum, L. D. Söderberg, S. V. Roth, *Macromolecules* **2019**, 52, 4721; b) W. Ohm, A. Rothkirch, P. Pandit, V. Körstgens, P. Müller-Buschbaum, R. Rojas, S. Yu, C. J. Brett, D. L. Söderberg, S. V. Roth, *J. Coat. Technol. Res.* **2018**, 15, 759.

[53] L. Yang, X. Jiang, W. Ruan, B. Zhao, W. Xu, J. R. Lombardi, *J. Raman Spectrosc.* **2009**, 40, 2004.

[54] X. J. L. Yang, W. Ruan, B. Zhao, W. Xu, J. R. Lombardi, *J. Phys. Chem. C* **2008**, 112, 20095.

[55] J. R. Lombardi, R. L. Birke, *J. Phys. Chem. C* **2014**, 118, 11120.

[56] H. Zhao, Y. Zhu, F. Li, R. Hao, S. Wang, L. Guo, *Angew. Chem. Int. Ed.* **2017**, 56, 8766.

[57] a) C. Ma, M. J. Trujillo, J. P. Camden, *ACS Appl. Mater. Interfaces* **2016**, 8, 23978; b) B. Fortuni, Y. Fujita, M. Ricci, T. Inose, R. Aubert, G. Lu, J. A. Hutchison, J. Hofkens, L. Latterini, H. Uji-i, *Chem. Commun.* **2017**, 53, 5121.

[58] G. Santoro, S. Yu, M. Schwartzkopf, P. Zhang, S. Koyiloth Vayalil, J. F. H. Risch, M. A. Rübhausen, M. Hernández, C. Domingo, S. V. Roth, *Appl. Phys. Lett.* **2014**, 104, 243107.

[59] C. Krywka, J. Keckes, S. Storm, A. Buffet, S. V. Roth, R. Döhrmann, M. Müller, *J. Phys. Conf. Ser.* **2013**, 425, 072021.

[60] G. Benecke, W. Wagermaier, C. Li, M. Schwartzkopf, G. Flucke, R. Hoerth, I. Zizak, M. Burghammer, E. Metwalli, P. Müller-Buschbaum, M. Trebbin, S. Förster, O. Paris, S. V. Roth, P. Fratzl, *J. Appl. Crystallogr.* **2014**, 47, 1797.

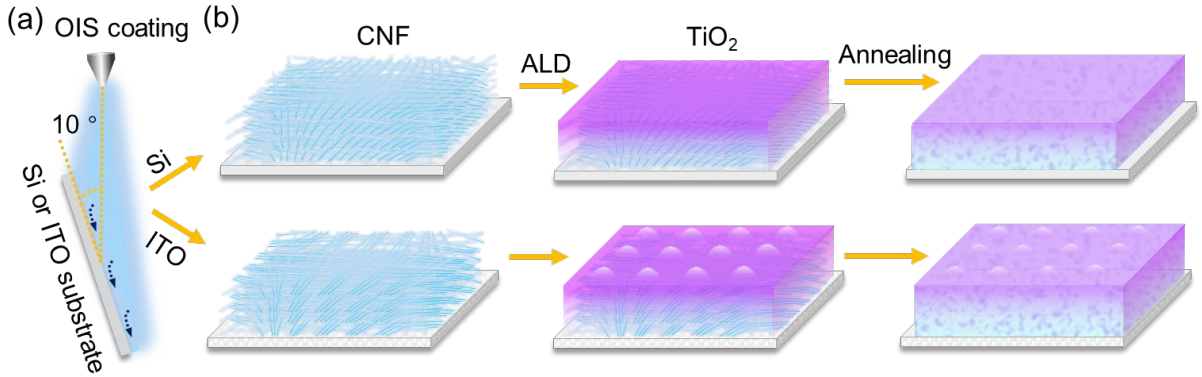

Figure 1. Fabrication of the titanium dioxide / cellulose nanofibril (TiO_2/CNF) composite films. (a) Preparation of CNF thin film through oblique incidence spraying (OIS) at an angle of 10°. (b) The as-prepared CNF thin film is composed of CNF matrix with a well-ordered network structure (left). TiO_2 nanoparticles (NPs) are coated by atomic layer deposition (ALD) onto CNF thin film with a thickness of δ_T = 10 nm and δ_T = 60 nm (middle). Samples with δ_T = 10 nm thickness are shown as an example. The ALD-coated TiO_2/CNF thin films are annealed at T = 450 ºC for 0.5 h to obtain a desired crystalline state (right). The upper and lower row indicate the fabrication of TiO_2/CNF thin films on Si and ITO, respectively.

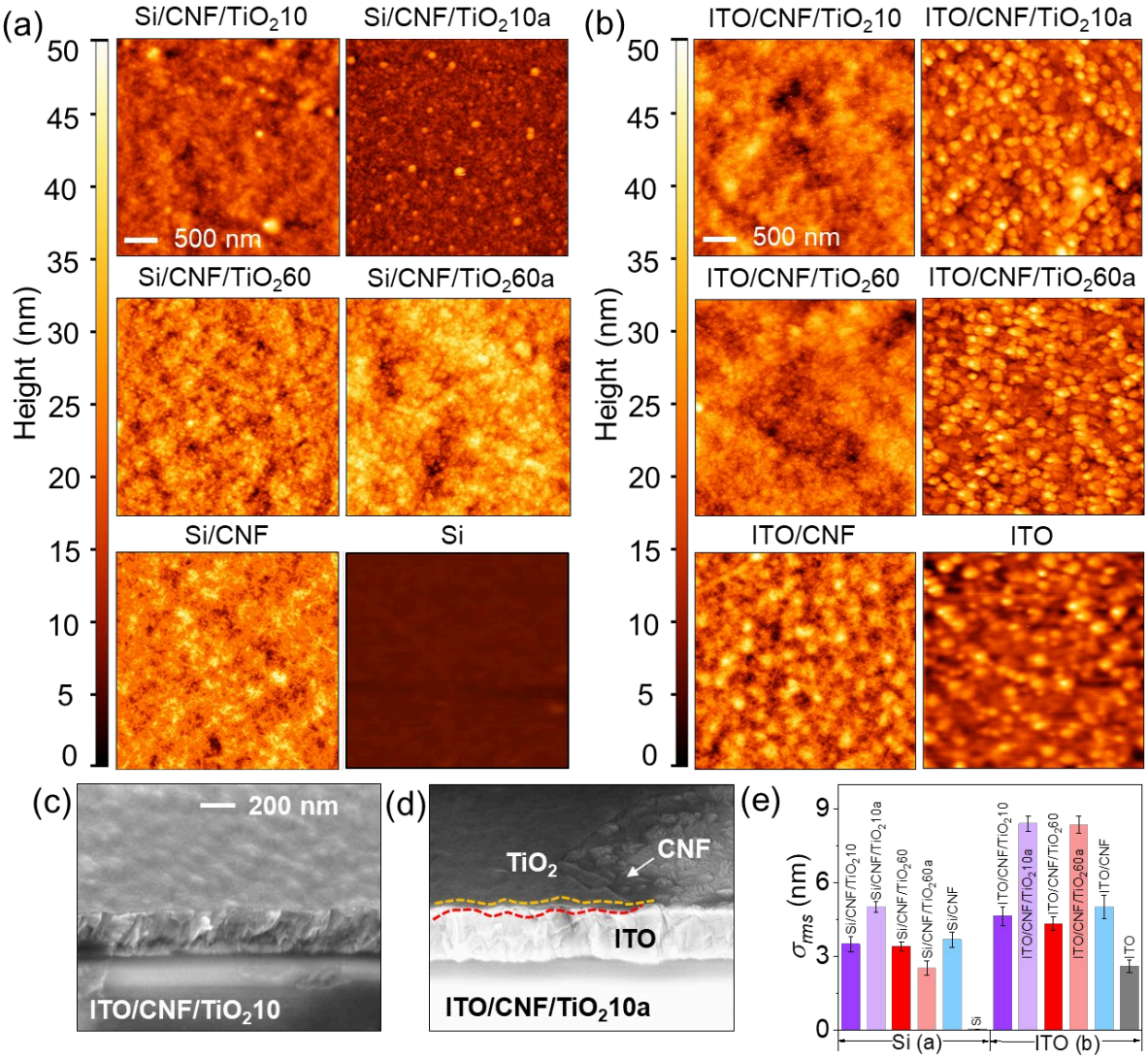

Figure 2. Morphology analysis of the TiO_2/CNF thin films. Atomic force microscopy (AFM) images of the TiO_2/CNF thin films on (a) Si and (b) ITO substrates, respectively. Abbreviations of the sample names are shown in **Table S1**. Taking the Si-based samples as an example, "Si" and "Si/CNF" represent the bare Si substrate and CNF thin film OIS-coated on Si substrate. "Si/CNF/$TiO_2$10" and "Si/CNF/$TiO_2$60" are samples with TiO_2 ALD-coated on the Si/CNF sample with δ_T = 10 nm and δ_T = 60 nm, respectively. "Si/CNF/$TiO_2$10a" and "Si/CNF/$TiO_2$60a" are the thermally-annealed "Si/CNF/$TiO_2$10" and "Si/CNF/$TiO_2$60" samples. (c, d) SEM cross-sectional images of the (c) ITO/CNF/$TiO_2$10 and (d) ITO/CNF/$TiO_2$10a samples showing the layer replication at the TiO_2 / CNF and the CNF / ITO interfaces. (e) Root-mean-square (RMS) roughness (σ_{rms}) analysis of the TiO_2/CNF thin films.

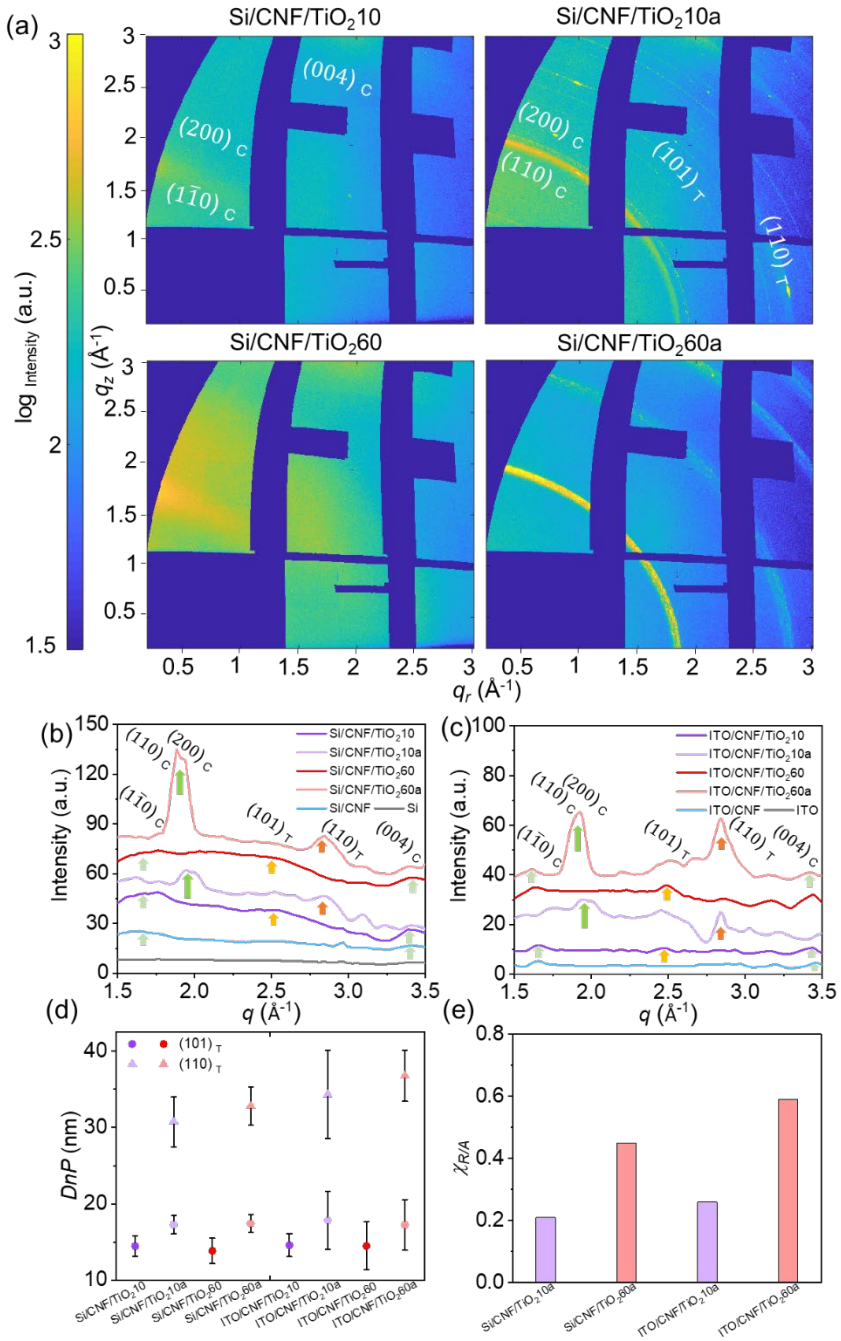

Figure 3. (a) 2D GIWAXS data (q_r, q_z maps) of the TiO_2/CNF thin films fabricated on Si. q_r, q_z maps of the ITO-based samples are shown in **Figure S9**. The scattering pattern of CNF and TiO_2 are designated with "C" and "T", respectively. (b, c) Radial integration of the reshaped q_r, q_z map of the (b) Si- and (c) ITO-based samples, respectively. Light-green and green arrows represent the crystalline patterns on type I and type II cellulose, respectively. light-orange and orange arrows show the crystalline patterns of amorphous / anatase TiO_2 and anatase / rutile TiO_2, respectively. (d) Crystalline domain size (*DnP*) of the anatase and rutile crystalline phase of TiO_2 calculated from the FHWM of the (101) and (110) peaks. (e) Crystalline phase ratio ($\chi_{R/A}$) of rutile to anatase TiO_2.

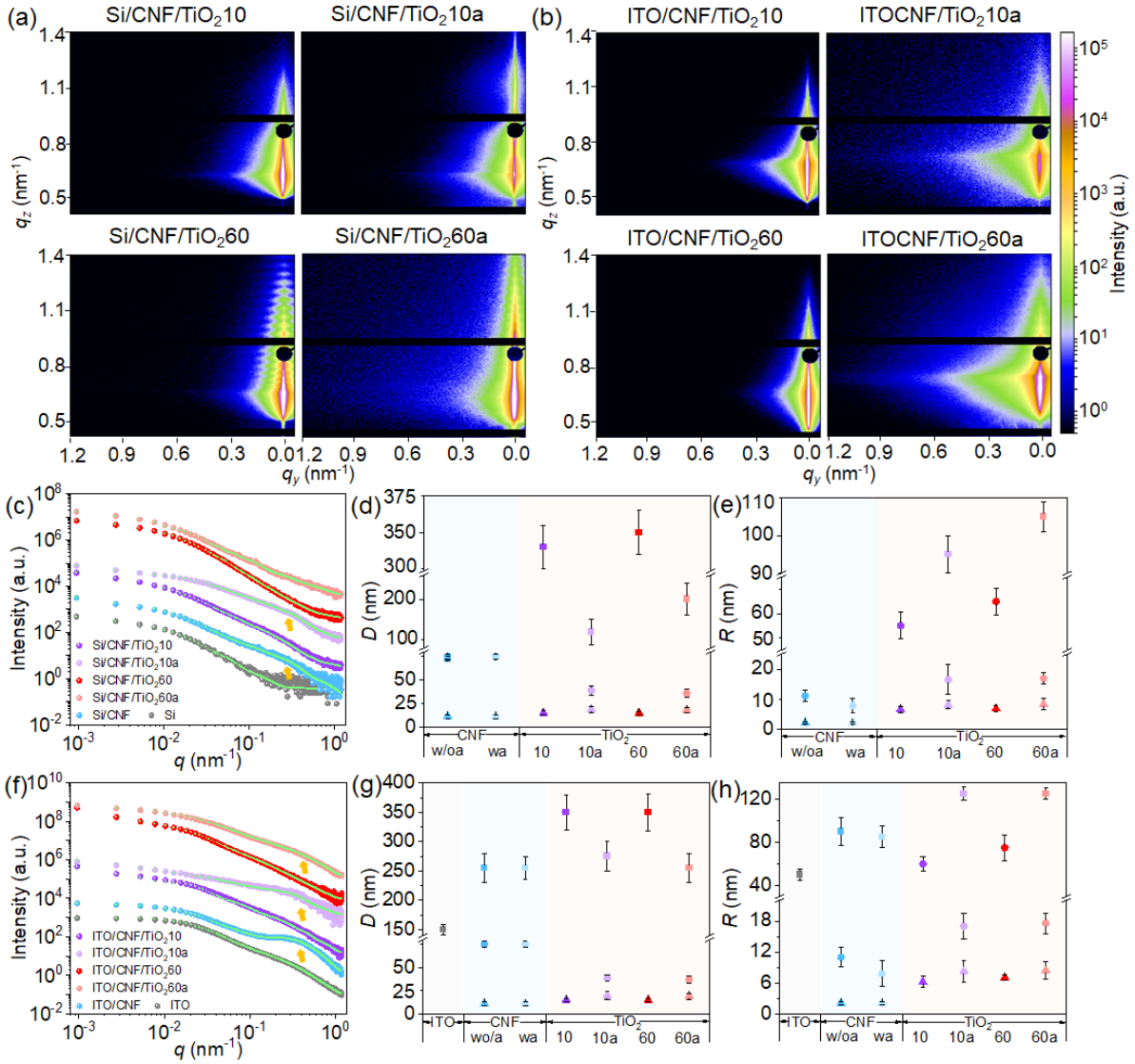

Figure 4. Topographical study of the TiO_2/CNF thin films at the nanoscale. (a,b) 2D GISAXS data of the TiO_2/CNF thin films on (a) Si and (b) ITO substrates, respectively. (c, f) Horizontal line-cuts of the 2D GISAXS data of the (c) Si- and (f) ITO-based samples, respectively. Details about the line-cut region is shown in **Figure S16**. The green dashed lines present the best fit to the data. (d, e, g, h) Extracted structure parameters for CNFs, TiO_2 and ITO (in g, h only). The fit method for the representative Si/CNF sample is shown in **Figure S17**. (d, g) Center-to-center distances (D) and (e, h) radii (R) of the ITO, CNF and TiO_2 nanostructures. The following symbols are used to represent the ITO, CNF, and TiO_2 nanostructures in TiO_2/CNF thin films for simplicity. "wo/a" and "wa" represent the CNF nanostructures before and after annealing. "10", "10a" represent TiO_2 nanostructures in samples (δ_T = 10 nm) before and after annealing, which correspond to the "Si or ITO/CNF/$TiO_2$10" and "Si or ITO/CNF/$TiO_2$10a" samples. "60" and "60a" represent TiO_2 nanostructures in samples (δ_T = 60 nm) before and after annealing, corresponding to the "Si or ITO/CNF/$TiO_2$60" and "Si or ITO/CNF/$TiO_2$60a" samples.

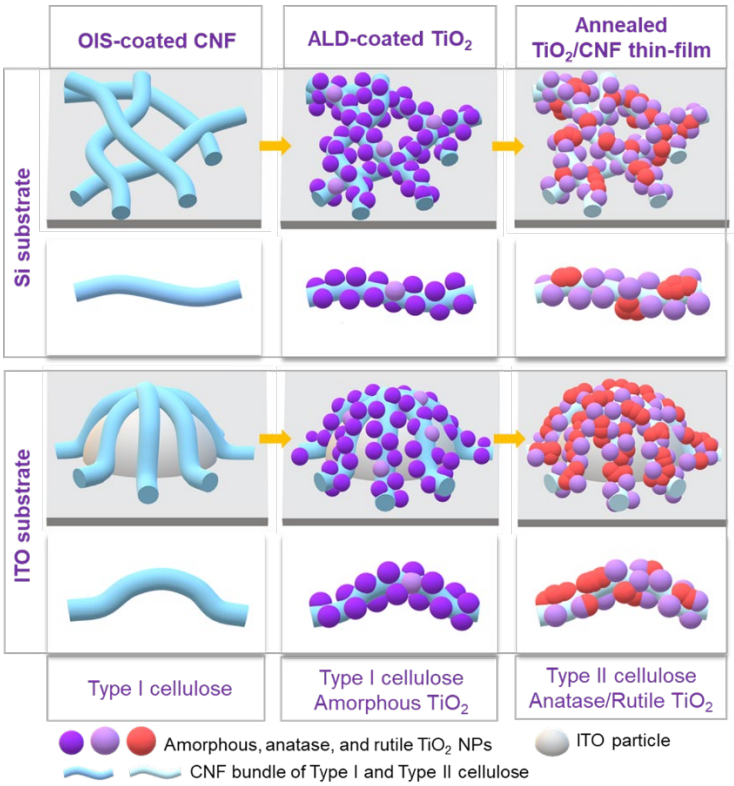

Figure 5. Schematic representation of the morphology and crystallinity evolution of TiO_2 and CNF nanostructures on Si (top) and ITO (bottom) substrates, respectively.

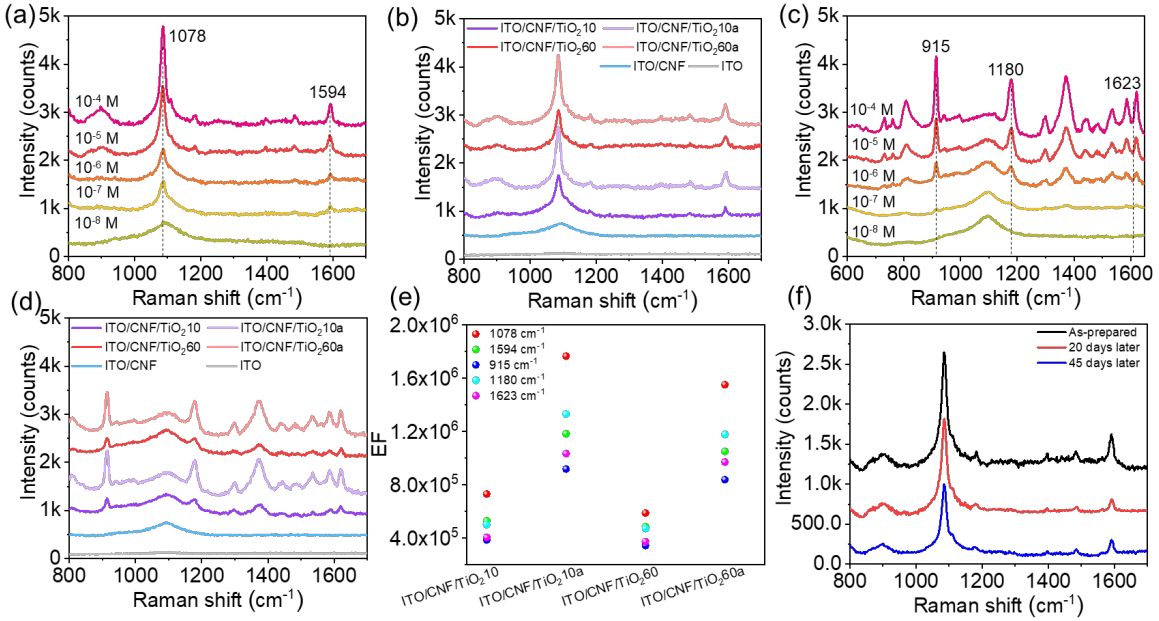

Figure 6. Evaluation on the potential of TiO_2/CNF thin films as a surface enhanced raman scattering (SERS) substrate. (a, c) SERS spectra of 4-mercaptobenzoic acid (4-MBA) and crystal violet (CV) at different concentrations (from 10^{-4} M to 10^{-8} M) on the Si/CNF/$TiO_2$10a sample. (b, d) SERS spectra of 10^{-5} M 4-MBA and 10^{-5} M CV on ITO-based samples. (e) Enhancement factor (EF) calculated from the two characteristic bands at 1078 cm^{-1} and 1594 cm^{-1} in 4-MBA spectra, and three characteristic bands at 915 cm^{-1}, 1180 cm^{-1} and 1623 cm^{-1} in CV spectra. (f) The SERS spectra of 10^{-5} M 4-MBA on the ITO/CNF/$TiO_2$10a sample after storing for 45 days.

The morphology and crystallinity of bio-templated and thermally-annealed titanium dioxide /cellulose nanofibril (TiO_2/CNF) thin films are studied by X-ray scattering techniques. The TiO_2 layer achieves a desired crystalline state while preserving the morphology of the CNF template. The resulting highly-ordered and polymorphous TiO_2/CNF thin films display an excellent SERS performance compared to semiconductor metal oxide nanomaterial-based SERS substrates.

Qing Chen, Marie Betker, Constantin Harder, Calvin J. Brett, Matthias Schwartzkopf, Nils Ulrich, Maria E. Toimil-Molares, Christina Trautmann, L. Daniel Söderberg, Christian L. Weindl, Volker Körstgens, Peter Müller-Buschbaum, Mingming Ma, and Stephan V. Roth**

Biopolymer-templated deposition of ordered and polymorph TiO_2 thin films for improved SERS sensitivity

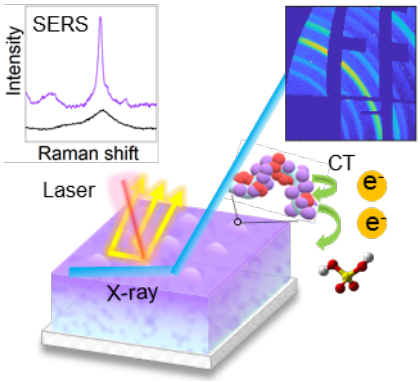

Supporting Information

Biopolymer-templated deposition of ordered and polymorph TiO_2 thin films for improved SERS sensitivity

Qing Chen, Marie Betker, Constantin Harder, Calvin J. Brett, Matthias Schwartzkopf, Nils Ulrich, Maria E. Toimil-Molares, Christina Trautmann, L. Daniel Söderberg, Christian L. Weindl, Volker Körstgens, Peter Müller-Buschbaum, Mingming Ma, and Stephan V. Roth**

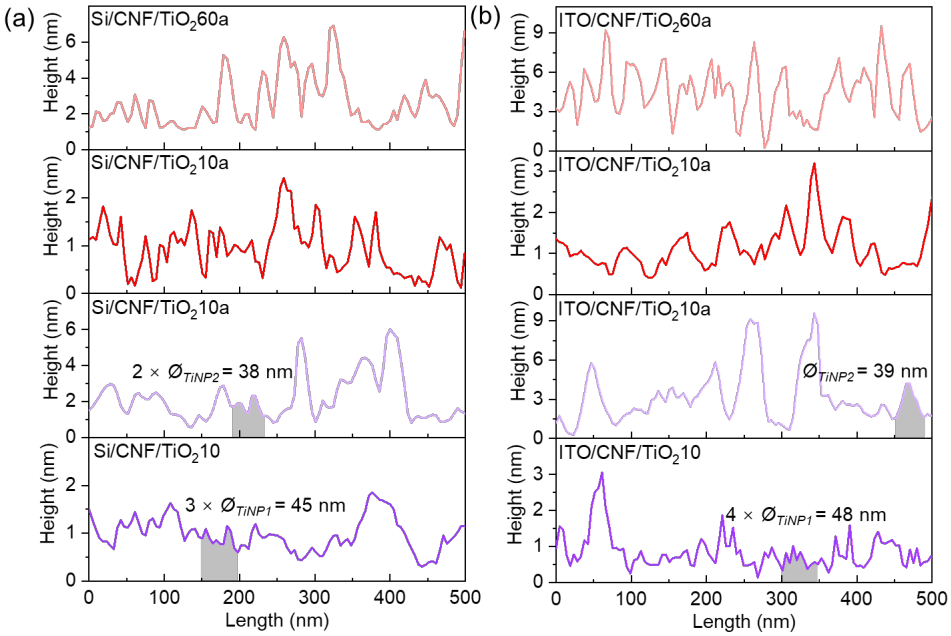

Figure S1. Average line-cut analysis of TiO_2/CNF thin films prepared on (a) Si and (b) ITO substrates. The dashed areas are selected as exemplary regions for the calculation of the diameter of TiO_2 ($Ø_{TiNP1}$ or $Ø_{TiNP2}$) by averaging the length of the continuously distributed TiO_2 nanostructures.

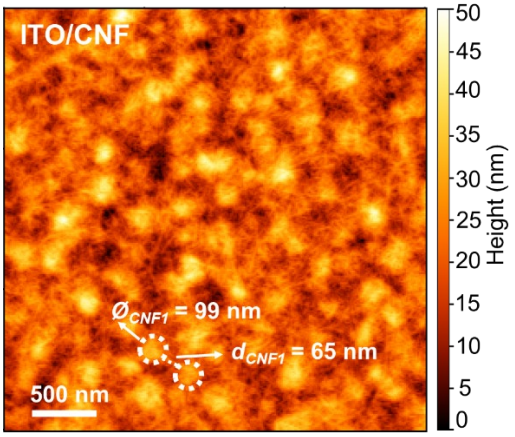

Figure S2. Enlarged AFM image showing the knot-like morphology of the CNF thin film fabricated on ITO (the ITO/CNF sample). The white dashed circles represent the diameter ($Ø_{CNF1}$) of the knots, and the white dashed line represents the edge-to-edge distance (d_{CNF1}) between the knots.

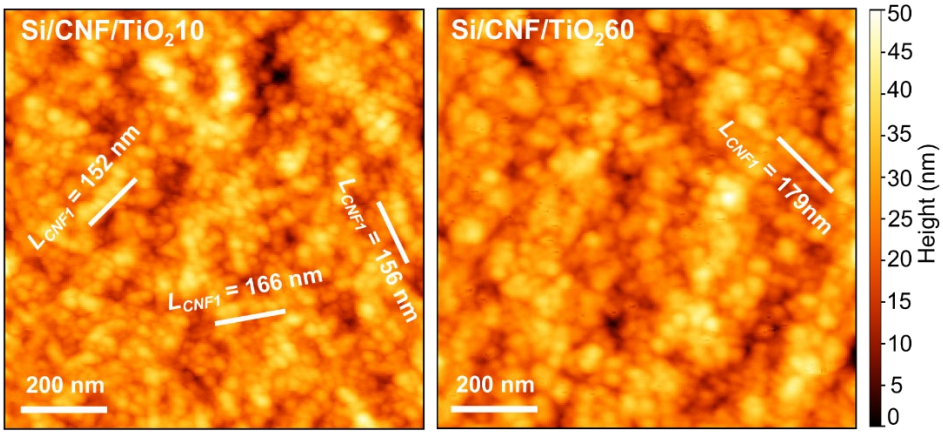

Figure S3. Enlarged AFM images showing the fibrous morphology in ALD-coated TiO_2/CNF thin films on Si (Si/CNF/$TiO_2$10 and Si/CNF/$TiO_2$60 samples), with the white solid lines showing the length scale (L_{CNF1}) of the replicated necklace architecture.

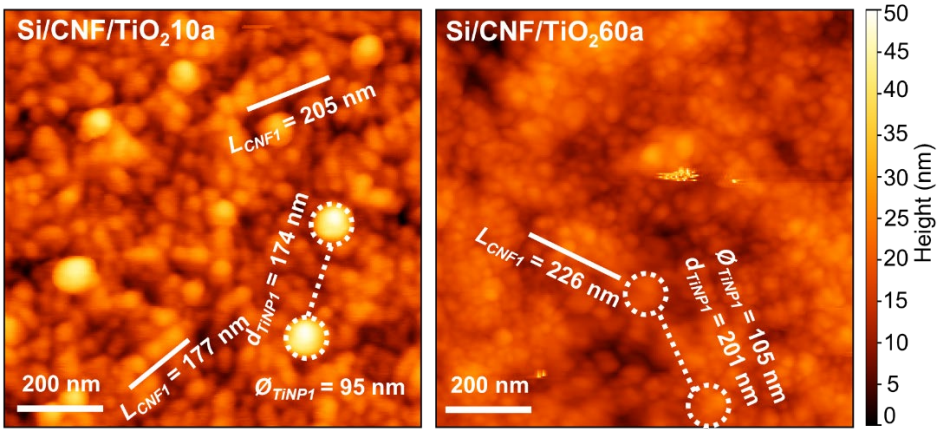

Figure S4. Enlarged AFM images showing the surface morphology of the thermally-annealed TiO_2/CNF thin films on Si (Si/CNF/$TiO_2$10a and Si/CNF/$TiO_2$60a samples). The solid white line represents the length scale (L_{CNF1}) of fibrous architecture, and the white dashed circles and lines represent the diameter ($Ø_{TiNP1}$) and edge-to-edge distance (d_{TiNP1}) of the TiO_2 agglomerates.

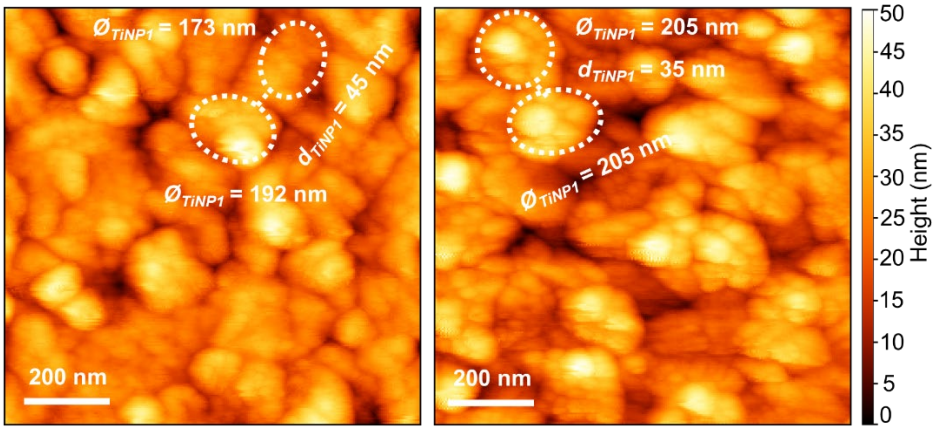

Figure S5. Enlarged AFM images show the terrace-morphology of the thermally-annealed TiO_2/CNF thin films on ITO (ITO/CNF/$TiO_2$10a and ITO/CNF/$TiO_2$60a samples). The white dashed circles and lines guide to the eye the diameter ($Ø_{TiNP1}$) and edge-to-edge distance (D_{TiNP1}) of the TiO_2 terrace.

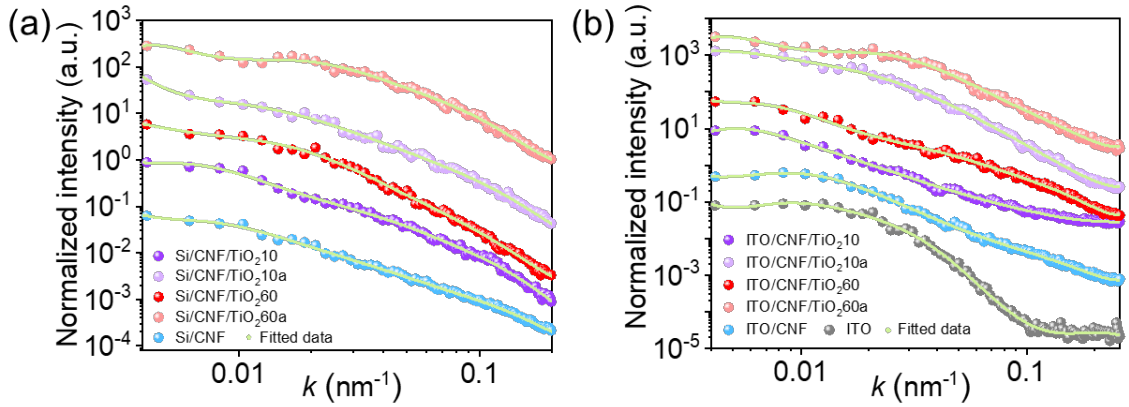

Figure S6. Power spectral density (PSD) distribution obtained from the AFM images of the (a) Si- and (b) ITO-based samples. The PSD signals are fitted with cylindrically shaped objects for CNFs and spherical objects for TiO_2, respectively. The curves are shifted vertically for clarity.

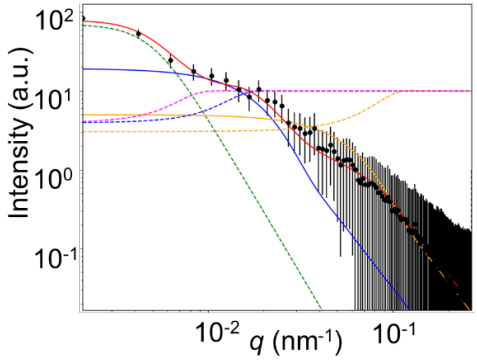

Figure S7. Example of the PSD fit of the Si/CNF/$TiO_2$60a samples. CNF is fitted with two cylindrical form factors and TiO_2 NPs are fitted with two spherical form factors. The green dashed line represents the resolution function. The solid blue and yellow lines are the form factors of the cylinders or spheres. The dashed blue and yellow lines represent the structure factors. The solid red line is the fit curve. The fit model has been established and verified in our previous studies as explained in the text. Hence, this model is sufficient for deriving the main morphological and structural features of the TiO_2/CNF thin films.

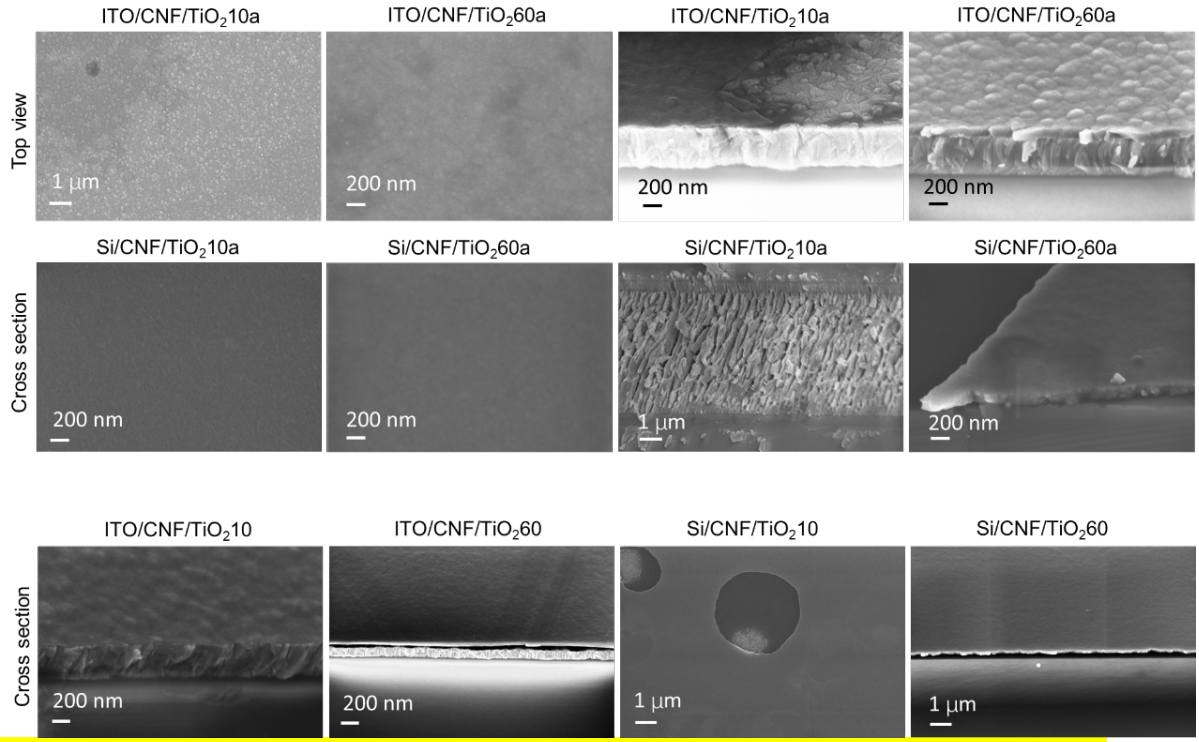

Figure S8. Top-view and / or cross-sectional SEM images of the TiO_2/CNF thin films.

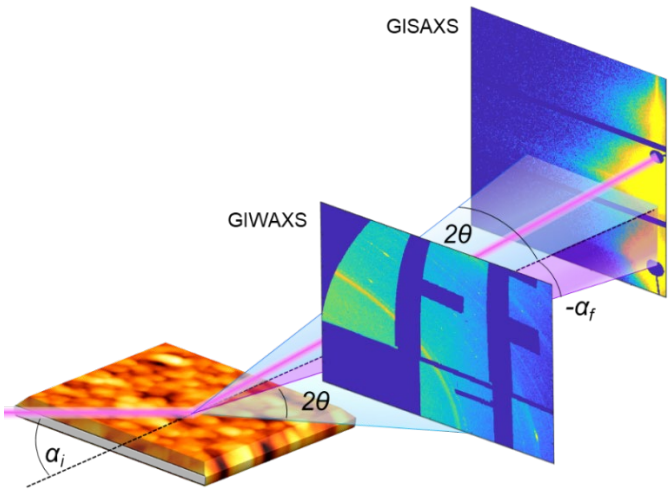

Figure S9. Sketch of the GISAXS and GIWAXS scattering geometry.

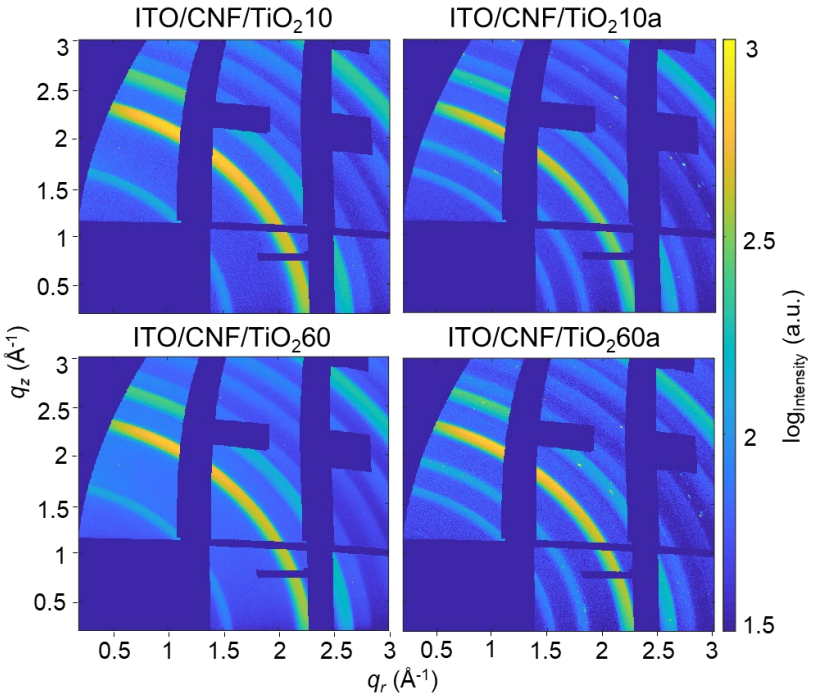

Figure S10. 2D GIWAXS data (q_r, q_z maps) of the TiO_2/CNF thin films on ITO substrates.

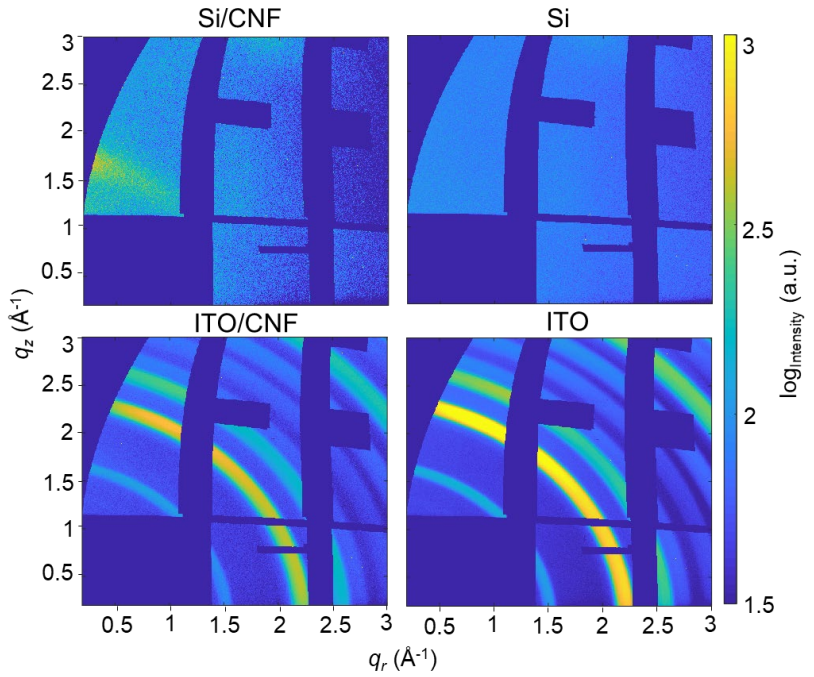

Figure S11. 2D GIWAXS data (q_r, q_z maps) of the CNF thin films and their corresponding substrates.

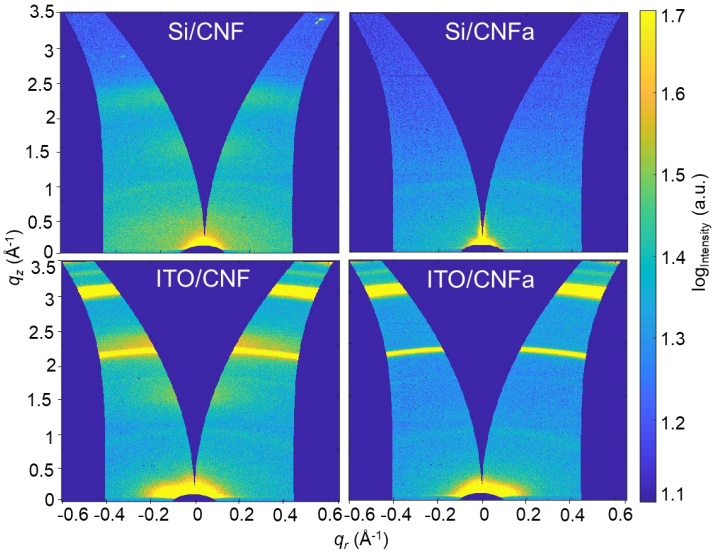

Figure S12. 2D GIWAXS data (q_r, q_z maps) of the pristine CNF thin films (without ALD-coated TiO_2) before (Si/CNF, ITO/CNF) and after (Si/CNFa, ITO/CNFa) thermal annealing.

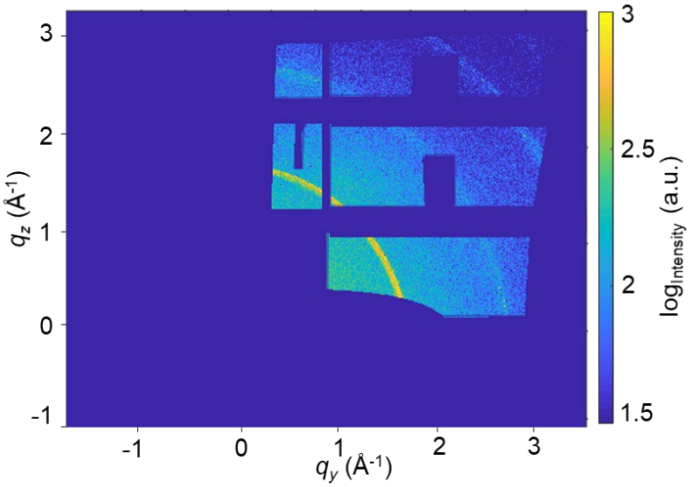

Figure S13. Radial-integration region in the GIWAXS analysis of the Si/CNF/$TiO_2$60a sample with a range as shown by the colored region ($0.5 < q_z < 3$ Å^{-1}, $0.5 < q_y < 3$ Å^{-1}, $0.5 < chi < 90°$).

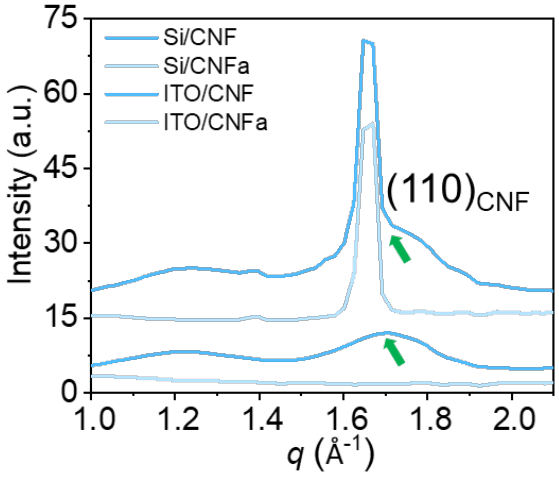

Figure S14. q plot from the radial integration of the pristine CNF thin films from **Figure S11**.

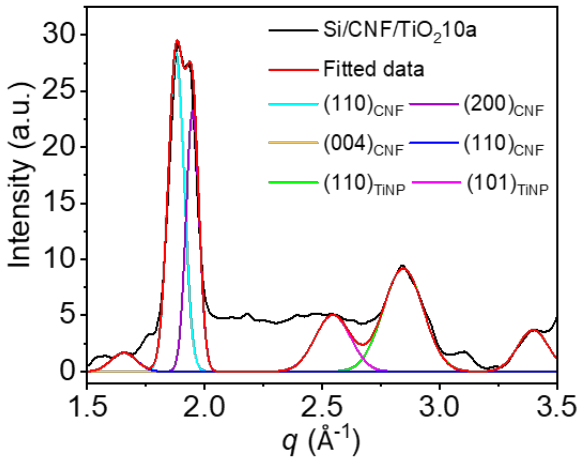

Figure S15. Gaussian fits of the Si/CNF/$TiO_2$60a sample showing the scattering patterns of CNFs and TiO_2.

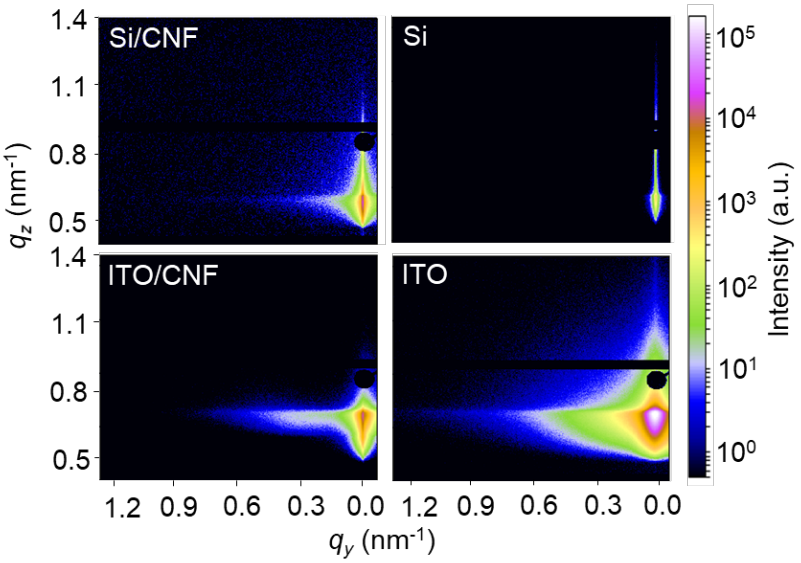

Figure S16. 2D GISAXS data of the CNF thin films and their corresponding substrates.

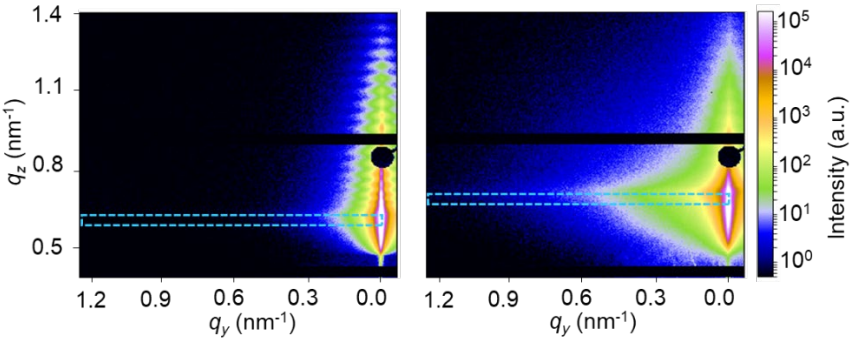

Figure S17. Horizontal line-cut regions in the 2D GISAXS data of the samples on Si (left) and ITO substrates (right), with the Si/CNF/$TiO_2$60 and ITO/CNF/$TiO_2$60 samples shown as examples, respectively.

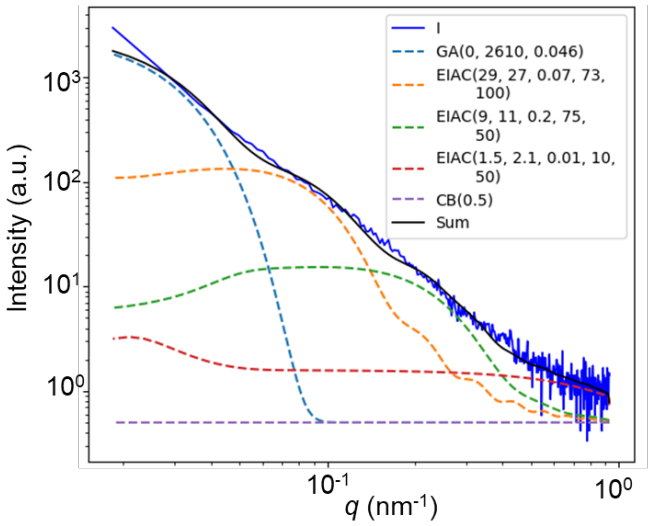

Figure S18. GISAXS fit based on the model as explained in the text with the CNF thin film (Si/CNF) as an example.

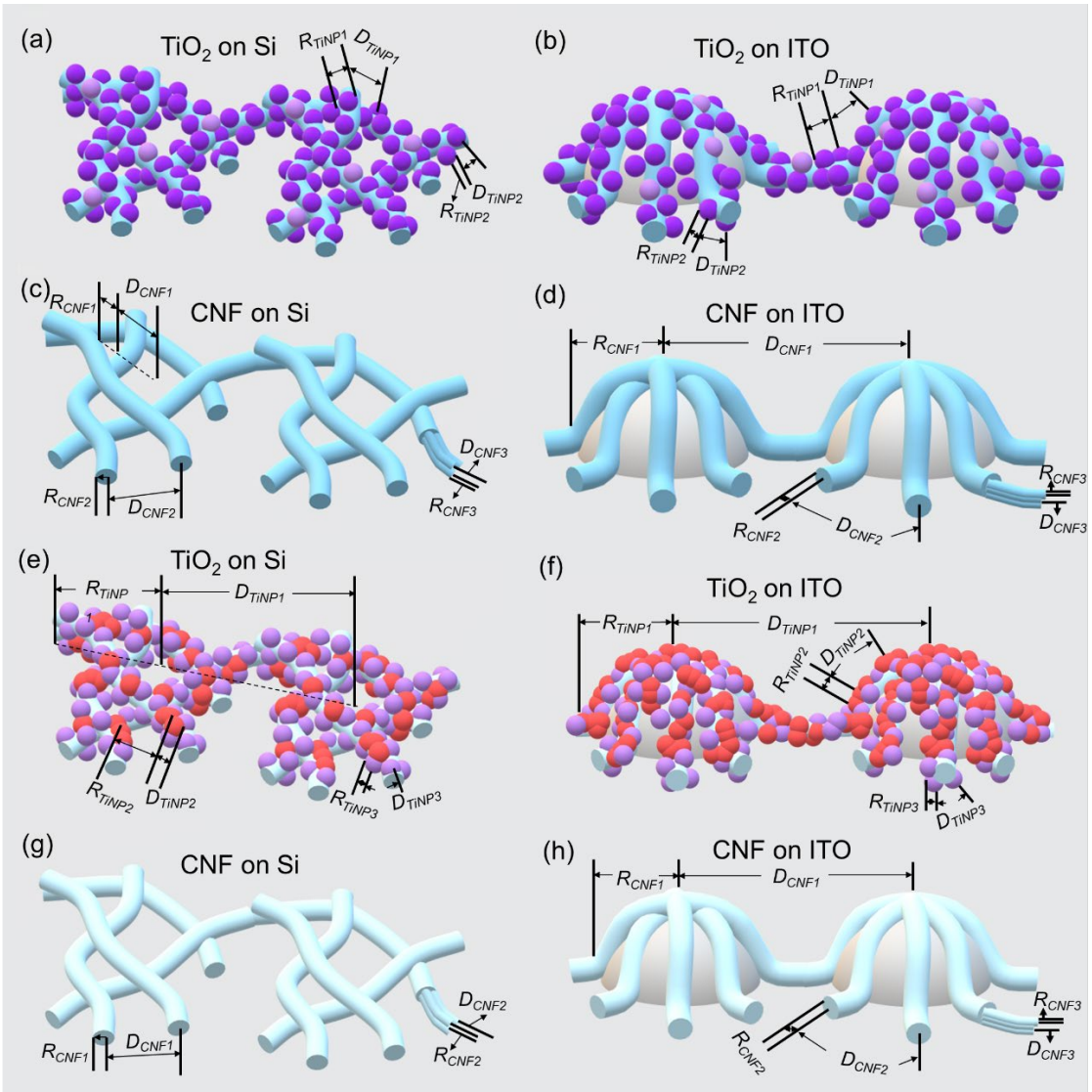

Figure S19. Extracted parameter of GISAXS data analysis for TiO_2 and CNFs before (a) and after (b) annealing. (a, b) Two TiO_2 nanostructures were identified for samples before annealing

(Si/CNF/$TiO_2$10, Si/CNF/$TiO_2$60, ITO/CNF/$TiO_2$10 and ITO/CNF/$TiO_2$60 samples), which is attributed to the individual (R_{TiNP2}, D_{TiNP2}) and agglomerates (R_{TiNP1}, D_{TiNP1}) of amorphous and anatase TiO_2 NPs. (e, f) After annealing, three nanostructures were extracted from GISAXS fitting (Si/CNF/$TiO_2$10a, Si/CNF/$TiO_2$60a, ITO/CNF/$TiO_2$10a and ITO/CNF/$TiO_2$60a samples), which we attributed to the individual form of anatase (R_{TiNP3}, D_{TiNP3}) and rutile (R_{TiNP2}, D_{TiNP2}) TiO_2 NPs, and the agglomerates of rutile TiO_2 NPs (R_{TiNP1}, D_{TiNP1}) based on the *DnP* analysis from GIWAXS and the observation of TiO_2 terrace from AFM observation. Samples on Si and ITO show identical TiO_2 nanostructures, despite the higher rutile-to-anatase ratio and relatively larger crystallite size of TiO_2 NPs on ITO substrates. (c, d) Three CNF nanostructures were identified for the samples before annealing (Si/CNF/$TiO_2$10, Si/CNF/$TiO_2$60, Si/CNF, ITO/CNF/$TiO_2$10, ITO/CNF/$TiO_2$60 and ITO/CNF samples). Despite the identical nanostructures attributing to the individual cellulose nanofibrils (R_{CNF3}, D_{CNF3}) and their bundles (R_{CNF2}, D_{CNF2}), the voids among the network of cellulose fibrils (R_{CNF1}, D_{CNF1}) were found on Si; and the knots of cellulose (R_{CNF1}, D_{CNF1}) were found on ITO, respectively. (g, h) After annealing, the nanostructures of cellulose nanofibrils (R_{CNF3}, D_{CNF3}) were preserved, but the cellulose bundles show a decreased R_{CNF2} with nearly identical D_{CNF2}, indicating a partial removal of the CNF template on both Si and ITO. However, the original nanostructure attributed to the voids among CNF network disappeared due to the recrystallization of TiO_2 NPs on Si. While on ITO, the CNF knots (R_{CNF1}, D_{CNF1}) is preserved due to the support of ITO.

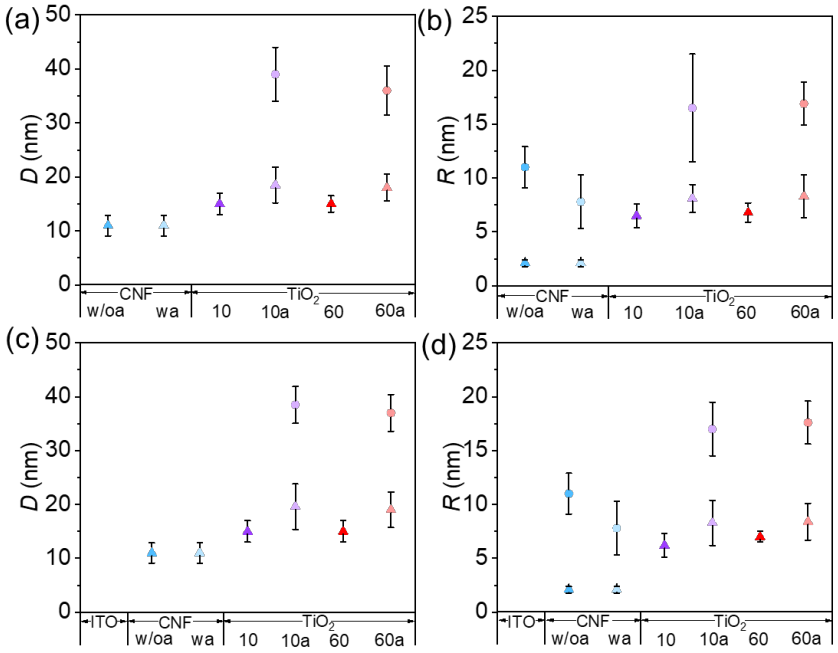

Figure S20. Zoomed-in fit parameters of the TiO_2/CNF thin films in the range of 0 nm < D < 50 nm and 0 < R < 25 nm. (a, b, c, d) correspond to the fit parameters in (d, e, g, h) of **Figure 3**, respectively. The following symbols are used to represent the ITO, CNF, and TiO_2 nanostructures in TiO_2/CNF thin films for simplicity. "wo/a" and "wa" represent the CNF nanostructures before and after annealing. "10", "10a" represent TiO_2 nanostructures in samples (δ_T = 10 nm) before and after annealing, which correspond to the "Si or ITO/CNF/$TiO_2$10" and "Si or ITO/CNF/$TiO_2$10a" samples. "60" and "60a" represent TiO_2 nanostructures in samples (δ_T = 60 nm) before and after annealing, corresponding to the "Si or ITO/CNF/$TiO_2$60" and "Si or ITO/CNF/$TiO_2$60a" samples.

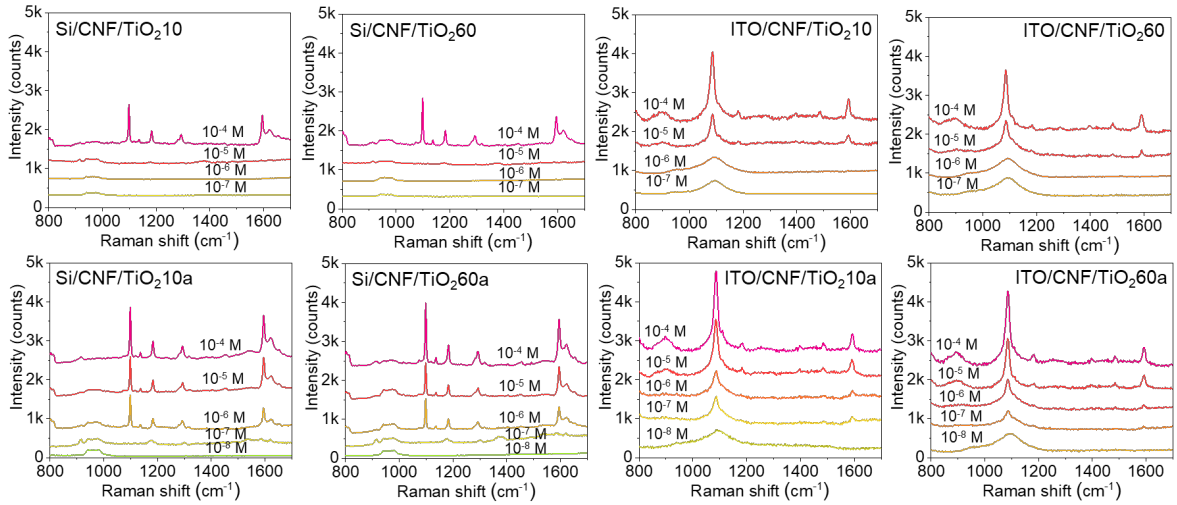

Figure S21. SERS spectra of TiO_2/CNF thin films on Si and ITO substrate at different concentrations of 4-MBA (from 10^{-4} M to10^{-8} M).

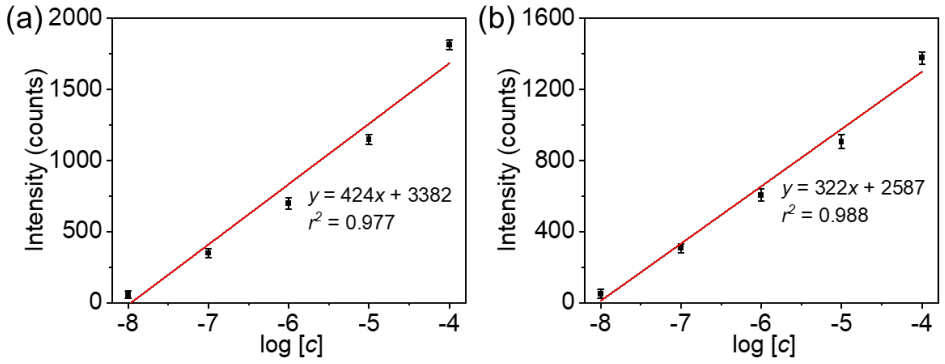

Figure S22. Plots of SERS intensities of the ITO/CNF/$TiO_2$10a sample with the increasing concentrations of 4-MBA and CV at (a) 1078 and (b) 915 cm^{-1}, respectively.

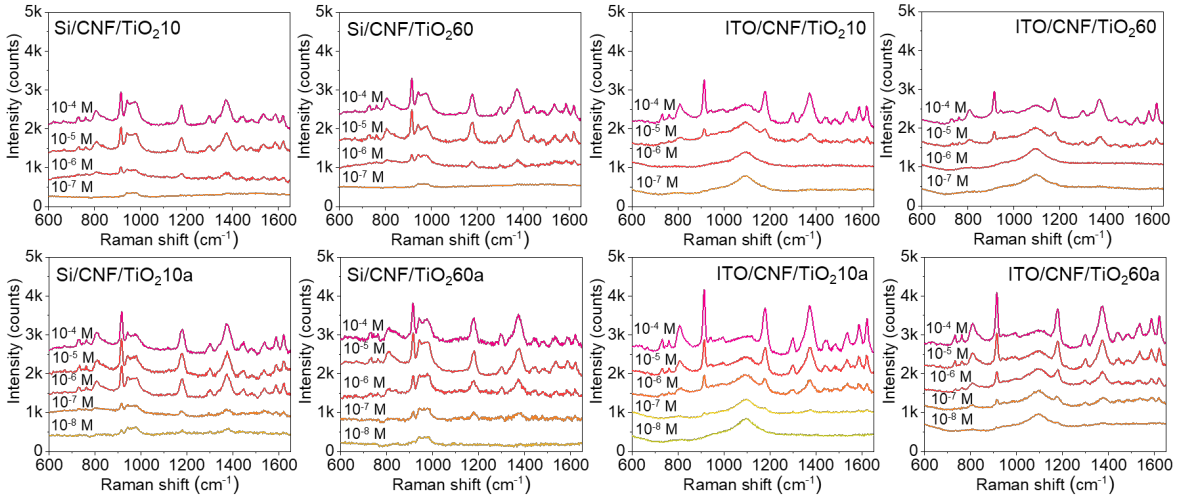

Figure S23. SERS spectra of TiO_2/CNF thin films on Si and ITO substrate at different concentrations of CV (from 10^{-4} M to10^{-8} M).

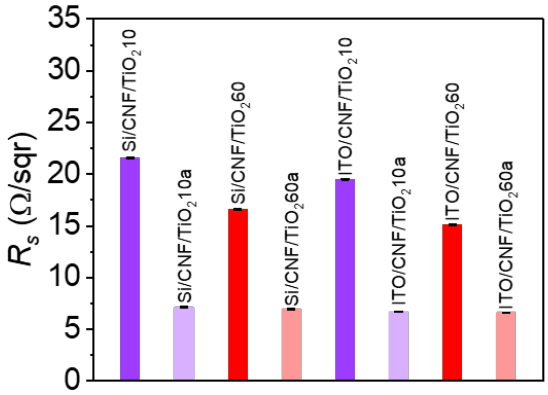

Figure S24. Sheet resistance (R_s) analysis of the TiO_2/CNF thin films.

Table S1. The abbreviations of each sample.

Samples on Si substrate (a)	**Abbreviations**
Si substrate	Si
CNF thin-film OIS-coated on Si substrate	Si/CNF
CNF thin-film OIS-coated on Si substrate after annealing (T = 450 ºC)	Si/CNFa
TiO_2 layer (δ_T = 10 nm) ALD-coated on the Si/CNF sample	Si/CNF/$TiO_2$10
TiO_2 layer (δ_T = 60 nm) ALD-coated on the Si/CNF sample	Si/CNF/$TiO_2$60
Si/CNF/$TiO_2$10 sample after annealing (T = 450 ºC)	Si/CNF/$TiO_2$10a
Si/CNF/$TiO_2$60 sample after annealing (T = 450 ºC)	Si/CNF/$TiO_2$60a
Samples on ITO substrate (b)	**Abbreviations**
ITO substrate	ITO
CNF thin-film OIS-coated on ITO substrate	ITO/CNF
CNF thin-film OIS-coated on ITO substrate after annealing (T = 450 ºC)	ITO/CNFa
TiO_2 ALD-coated on the b5 sample (δ_T=10 nm)	ITO/CNF/$TiO_2$10
TiO_2 ALD-coated on the b5 sample (δ_T=60 nm)	ITO/CNF/$TiO_2$60
Thermally-annealed b1 sample (T = 450 ºC)	ITO/CNF/$TiO_2$10a
Thermally-annealed b2 sample (T = 450 ºC)	ITO/CNF/$TiO_2$60a

Table S2. PSD fitting results of the Si- and ITO-based samples. *R* and *D* represents the radii (*R*) of and center-to-center distance (*D*) between the nanostructures, with $R = Ø / 2$, and $D = 2 \times R + d$ with respect to the line-cut results. The two nanostructures (R_{TiNP1}, D_{TiNP1}) and (R_{TiNP2}, D_{TiNP2}) refer to TiO_2 in the ALD-coated samples; and refers to CNF in Si/CNF and ITO/CNF samples.

Samples	R_{TiNP1} (nm)	D_{TiNP1} (nm)	R_{TiNP2} (nm)	D_{TiNP2} (nm)
Si/CNF/$TiO_2$10			59 ± 9	295 ± 55
Si/CNF/$TiO_2$60			57 ± 8	305 ± 58
Si/CNF/$TiO_2$10a	71 ± 15	247 ± 55	21 ± 10	41 ± 9
Si/CNF/$TiO_2$60a	70 ± 18	247 ± 62	21 ± 10	40 ± 9
ITO/CNF/$TiO_2$10			59 ± 9	295 ± 49
ITO/CNF/$TiO_2$60			57 ± 8	305 ± 55
ITO/CNF/$TiO_2$10a	77 ± 11	247 ± 55	21 ± 10	41 ± 8
ITO/CNF/$TiO_2$60a	75 ± 12	243 ± 32	21 ± 10	40 ± 8
	R_{CNF1} (nm)	D_{CNF1} (nm)	R_{CNF2} (nm)	D_{CNF2} (nm)
Si/CNF	27 ± 4	73 ± 12	9 ± 3	75 ± 15
ITO/CNF	79 ± 9	245 ± 39	9 ± 3	75 ± 15

Table S3. Surface area of the Si- and ITO-based samples obtained from the Gwyddion software v 2.55 at a scan size of 3 × 3 μm^2.

Samples	Surface area (μm^2)	Samples	Surface area (μm^2)
Si/CNF/$TiO_2$10	0.037	ITO/CNF/$TiO_2$10	0.138
Si/CNF/$TiO_2$60	0.032	ITO/CNF/$TiO_2$60	0.071
Si/CNF/$TiO_2$10a	0.055	ITO/CNF/$TiO_2$10a	0.298
Si/CNF/$TiO_2$60a	0.057	ITO/CNF/$TiO_2$60a	0.472
Si/CNF	0.042	CNF/ITO	0.146
Si	0.007	ITO	0.016

Table S4. Functions and corresponding abbreviations in GISAXS fit.

Function	Abbreviation
Gaussian peak	GA
Effective interface approximation sphere	EIAS
Effective interface approximation cylinder	EIAC
Constant background	CB
Raw data	I
Fitted data	Sum

Table S5. The radii "*R*" of CNF (R_{CNF1}, R_{CNF2} and R_{CNF3}) and TiO_2 (R_{TiNP1}, R_{TiNP2} and R_{TiNP3}) extracted from GISAXS fitting.

Fits	R_{ITO} (nm)	R_{CNF1} (nm)	R_{CNF2} (nm)	R_{CNF3} (nm)	R_{TiNP1} (nm)	R_{TiNP2} (nm)	R_{TiNP3} (nm)
Si/CNF/$TiO_2$10		27 ± 3	11.0 ± 1.9	2.1 ± 0.3	55 ± 6	6.5 ± 1.1	
Si/CNF/$TiO_2$60		27 ± 3	11.0 ± 1.9	2.1 ± 0.3	66 ± 6	6.8 ± 0.9	
Si/CNF/$TiO_2$10a			7.8 ± 2.5	2.1 ± 0.3	95 ± 5	16.5 ± 2.5	8.1 ± 1.3
Si/CNF/$TiO_2$60a			7.8 ± 2.5	2.1 ± 0.3	105 ± 4	16.9 ± 2.0	8.3 ± 2.0
Si/CNF		27 ± 3	11.0 ± 1.9	2.1 ± 0.3			
ITO/CNF/$TiO_2$10	50 ± 5	90 ± 13	11.0 ± 1.9	2.1 ± 0.3	60 ± 7	6.2 ± 1.1	
ITO/CNF/$TiO_2$60	50 ± 5	90 ± 13	11.0 ± 1.9	2.1 ± 0.3	75 ± 12	7.0 ± 0.5	
ITO/CNF/$TiO_2$10a	50 ± 5	85 ± 10	7.8 ± 2.5	2.1 ± 0.3	113 ± 5	17.0 ± 2.5	8.3 ± 2.1
ITO/CNF/$TiO_2$60a	50 ± 5	85 ± 10	7.8 ± 2.5	2.1 ± 0.3	125 ± 3	17.6 ± 2.0	8.4 ± 1.7
CNF/ITO	50 ± 5	90 ± 13	11.0 ± 1.9	2.1 ± 0.3			
ITO	50 ± 5						

Table S6. The center-to-center distance "*D*" of CNF (D_{CNF1}, D_{CNF2} and D_{CNF3}) and TiO_2 (D_{TiNP1}, D_{TiNP2} and D_{TiNP3}) extracted from GISAXS fitting.

Fits	D_{ITO} (nm)	D_{CNF1} (nm)	D_{CNF2} (nm)	D_{CNF3} (nm)	D_{TiNP1} (nm)	D_{TiNP2} (nm)	D_{TiNP3} (nm)
Si/CNF/$TiO_2$10		73 ± 2	75 ± 3	11.0 ± 0.9	340 ± 10	15.5 ± 2.1	
Si/CNF/$TiO_2$60		73 ± 2	75 ± 3	11.0 ± 0.9	350 ± 15	15.5 ± 1.5	
Si/CNF/$TiO_2$10a			75 ± 3	11.0 ± 0.9	180 ± 8	39 ± 5	18.5 ± 3.3
Si/CNF/$TiO_2$60a			75 ± 3	11.0 ± 0.9	200 ± 10	36 ± 5	18.0 ± 2.5
Si/CNF		73 ± 2	75 ± 3	11.0 ± 0.9			
ITO/CNF/$TiO_2$10	150 ± 9	255 ± 20	75 ± 3	11.0 ± 0.9	350 ± 30	15.0 ± 2.1	
ITO/CNF/$TiO_2$60	150 ± 9	255 ± 20	75 ± 3	11.0 ± 0.9	350 ± 32	15.0 ± 2.1	
ITO/CNF/$TiO_2$10a	150 ± 9	123 ± 5	75 ± 3	11.0 ± 0.9	275 ± 25	39 ± 3	19.6 ± 4.2
ITO/CNF/$TiO_2$60a	150 ± 9	123 ± 5	75 ± 3	11.0 ± 0.9	255 ± 25	37 ± 3	19.0 ± 3.2
CNF/ITO	150 ± 9	255 ± 20	75 ± 3	11.0 ± 0.9			
ITO	150 ± 9						

Table S7. Comparison of the morphological parameters extracted from AFM linecut, AFM PSD fitting, GIWAXS and GISAXS fitting of the ITO/CNF/$TiO_2$10a sample.

	R_{TiNP1} (nm)	D_{TiNP1} (nm)	R_{TiNP2} (nm)	D_{TiNP2} (nm)	R_{TiNP3} (nm)	D_{TiNP3} (nm)
AFM linecut	97 ± 22		17 ± 5			
AFM PSD fitting	77 ± 11	247 ± 55	21 ± 10	41 ± 8		
GIWAXS fitting			18.4 ± 3.2		8.6 ± 3.3	
GISAXS fitting	113 ± 5	275 ± 25	17.0 ± 2.5	39 ± 3	8.3 ± 2.1	19.6 ± 4.2

Table S8. Raman shifts and assignments within the range of 700 ~ 1700 cm^{-1}.

Composition	Raman shift	Assignment	Ref
4-MBA	1594 s	*v*CC	[1]
	1182 w	*v*CH	
	1148 vw	*v*CH	
	1078 m	*v*CC	
CV	1623 s	*v*CC	[2]
	1377 m	*v*CC	
	1180 m	*ip*CH	
	915 s	*v*CC	
CNF	1097 m	*v*CC *v*CO	[3]

* v: stretch vibration; ip: in-plane vibration.
* s: strong, m: medium, w: weak, vw: very weak.

Table S9. Enhancement factor of the TiO_2 -based semiconductor SERS probes in literature.

Material composition	Fabrication technique	Analyte	*c* (M)	λ_{ex} (nm)	EF	Mechanism of enhancement	Ref
TiO_2 thin-film	Electrochemical anodization	Cyt b_5	2.5×10^{-5}	413	8.6	Electron transfer	[3]
PPy/CNT/TiO_2	Carbonization, solvothermal synthesis	MB	1.0×10^{-4}	532	3.0×10^{3}	Helical structures of CNT	[4]
TiO_2 microarray	TiO_2 casting on PS film, anneal at 450 °C	MB	1.0×10^{-3}	532	2.0×10^{4}	Multiple light scattering	[5]
TiO_2 spherical resonators	TiO_2 ALD-coated on SiO_2 NPs, anneal at 700 °C	MB	1.0×10^{-5}	633	Not defined	Refractive index, light scattering and geometry	[6]
Core-shell TiO_2 NPs	TiO_2 mixing with $NaBH_4$; anneal at 350 °C	4-NBT	5.0×10^{-4}	532	4.3×10^{5}	PICT	[7]
TiO_2 thin-film	N^+ ion irradiation; vacuum-anneal at 500 °C	R6G	5.0×10^{-8}	532	4.5×10^{5}	CT	[8]
Sea urchin-like TiO_2	Hydrothermal assisted self-assembly	DA	5.0×10^{-4}	532	1.6×10^{6}	CT, EM	[9]
TiO_2 nanosheets	Synthesis on GO nanosheet; anneal at 400, 650 °C	4-MBA	1.0×10^{-4}	633	1.9×10^{6}	PICT	[10]
TiO_2/CNF/ITO	TiO_2 ALD-coated on CNFs, anneal at 450 °C	4-MBA	1.0×10^{-5}	532	1.8×10^{6}	CT, light scattering	This
TiO_2/CNF/Si	TiO_2 ALD-coated on CNFs, anneal at 450 °C	4-MBA	1.0×10^{-5}	532	5.3×10^{5}	CT, light scattering	work

* *c* (M) and λ_{ex} (nm) are the concentration of analyte, and excitation wavelength at which the SERS spectra is measured for the calculation of EF values.
* Abbreviations: Cyt: cytochrome; PPy: polypyrrole; CNT: carbonaceous nanotubes; MB: methylene blue; PS: polystyrene; ALD: atomic layer deposition; NP: nanoparticle; 4-NBT: 4-nitrobenzenethiol; PICT: photon-induced charge transfer; R6G: rhodamine 6G; CT: charge transfer; DA: dopamine; EM: electromagnetic; GO: graphene oxide; 4-MBA: 4-mercaptobenzoic acid; CNF: cellulose nanofibrils.

Note to the annealing condition

We annealed the TiO_2/CNF thin films under 450 ºC for 0.5 h due to the following reasons. The crystallinity of TiO_2 for SERS enhancement of the surface-adsorbed molecules is a ‘‘double-edged sword’’. It is important to achieve a larger crystalline size of the anatase phase and a higher surface defect content simultaneously, which can be controlled using a suitable calcination temperature. We choose the annealing temperature of 450 ºC according to literature [11,12] to ensure that the crystalline state of TiO_2, which stays in anatase phase and start to transform into the rutile phase. For the stability of CNF, we proposed that the ALD-coated TiO_2 layer could protect the CNF from carboxylation and therefore the template morphology is retained after annealing. This is verified by the (200) and (110) scattering peaks from the

GIWAXS, reduced radii of cellulose bundles (7.8 ± 2.5 nm) from GISAXS fitting, and the necklace architecture of TiO_2 NPs from AFM analysis. These results demonstrate that CNFs are not fully carbonized but reduced in the radius and increased in thermal stability. Collectively, the annealing temperature at 450 ºC is suitable for the morphological and crystalline evolution of TiO_2 NPs for SERS applications.

Note to the GIWAXS measurement

We used GIWAXS for studying the crystalline state of TiO_2 and CNF due to the following reasons. Although the 2-theta X-ray analysis (like WAXS) might be more familiar to readers, GIWAXS analysis is fully sufficient to summarize the data since it maximizes the signal strength due to the thickness (210 nm < δ < 260 nm) of our samples [13]. Peak positions in a GIWAXS provide information about crystalline dimensions in reciprocal space [14], while the intensity of peaks can be used to quantitatively study the degree of crystallinity and the phase ratio in polymorphous thin films [15].

Supplementary references

[1] X. Xue, W. Ji, Z. Mao, H. Mao, Y. Wang, X. Wang, W. Ruan, B. Zhao, J. R. Lombardi, *J. Phys. Chem. C* **2012**, 116, 8792.

[2] D. Maznichenko, K. Venkatakrishnan, B. Tan, *J. Phys. Chem. C* **2012**, 117, 578.

[3] X. Han, C. Kohler, J. Kozuch, U. Kuhlmann, L. Paasche, A. Sivanesan, M. Weidinger, P. Hildebrandt, *Small* **2013**, 9, 24, 4175.

[4] B. Qiu, M. Xing, Q. Yi, J. Zhang, *Angew. Chem. Int. Ed.* **2015**, 54, 10643.

[5] D. Qi, L. Lu, L. Wang, J. Zhang, *J. Am. Chem. Soc.* **2014**, 136, 9886.

[6] I. Alessandri, *J. Am. Chem. Soc.* **2013**, 135, 5541.

[7] J. Lin, W. Ren, A. Li, C. Yao, T. Chen, X. Ma, X. Wang, A. Wu, *ACS Appl. Mater. Interfaces* **2020**, 12, 4204.

[8] X. Zheng, F. Ren, S. Zhang, X. Zhang, H. Wu, X. Zhang, Z. Xing, W. Qin, Y. Liu, C. Jiang, *ACS Appl. Mater. Interfaces* **2017**, 9, 14534.

[9] Y. Yu, J. Du, C. Jing, *J. Mater. Chem. C*, **2019**, 7, 14239.

[10] X. Wang, W. Shi, S. Wang, H. Zhao, J. Lin, Z. Yang, M. Chen, L. Guo, *J. Am. Chem. Soc.* **2019**, 141, 5856.

[11] I. S. Cho, Z. Chen, A. J. Forman, D. R. Kim, P. M. Rao, T. F. Jaramillo, X. Zheng. Nano Lett. 2011, 11, 4978

[12] R. Tao, J. Wu, H. Xue, X. Song, X. Pan, X. Fang, X. Fang, S. Dai. J. Power Sources 2010, 195, 2989

[13]. Q. Chen, C. J. Brett, A. Chumakov, M. Gensch, M. Schwartzkopf, V. Körstgens, L. D. Söderberg, A. Plech, P. Zhang, P. Müller-Buschbaum, S. V. Roth. ACS Appl. Nano Mater., 2021, 4, 503-513.

[14] V. Savikhin, H. Steinrück, R. Liang, B. A. Collins, S. D. Oosterhout, P. M. Beaujuged, M. F. Toney. J. Appl. Cryst. 2020. 53

[15] S. D. Oosterhout, V. Savikhin, J. Zhang, Y. Zhang, M. A. Burgers, S. R. Marder, G. C. Bazan, M. F. Toney. Chem. Mater. 2017, 29, 3062-3069